science.sciencemag.org/content/370/6518/837/suppl/DC1

Supplementary Materials for

Astronomical context of Solar System formation from molybdenum isotopes in meteorite inclusions

Gregory A. Brennecka*, Christoph Burkhardt, Gerrit Budde, Thomas S. Kruijer, Francis Nimmo, Thorsten Kleine

*Corresponding author. Email: brennecka2@llnl.gov

Published 13 November 2020, *Science* **370**, 837 (2020)
DOI: 10.1126/science.aaz8482

This PDF file includes:

Materials and Methods
Supplementary Text
Figs. S1 to S7
Tables S1 to S6
References

Materials and Methods

Investigated CAI samples

We utilized as broad a representation of the known CAI population as feasible. Included were CAIs that had been measured for other isotopic systems to allow integrated isotopic information. As such, many of the samples used in this study were previously described in the literature (*i.e.*, *12, 15, 18, 25, 33, 34*). The relevant isotopic data from these prior studies, additional isotopic systems measured for this study on the same samples, and additional samples specific to this study are provided in tables S1 to S6 and figures S1 to S7. In previous studies (*e.g. 33*) CAIs were referred as either coarse-grained or fine-grained types. In this study, all CAIs with unfractionated REE are coarse grained with exception of CAI A-ZH-5 which is fine-grained, and all CAIs with group II patterns are fine-grained with the exception of CAI AI02, which is coarse grained.

Petrographic information

Whereas petrography for many CAIs of this study have previously been reported in the literature, CAIs BB8 and R2 have not been previously described, and exhibit two very different Δ^{95}Mo values. Both BB8 and R2 are unfractionated CAIs, having flat REE patterns. Petrographically, the samples are both coarse-grained Type B CAIs. Back-scattered electron and Ca-Mg-Al overlay images for these two samples are provided in Fig S1.

CAI BB8 is a typical coarse-grained sample with mineralogy that includes melilite, pyroxene, and spinel. Minor secondary mineralization occurs along melilite grain boundaries. CAI R2 contains abundant melilite and spinel, exhibiting some secondary nepheline and sodalite on the rim. In addition, R2 contains olivine—a less refractory phase not present in high abundance in many other CAIs.

Sample preparation and digestion

The newly investigated CAIs (CAI 2a, CAI 12, CAI 17a, CAI 43, 3PO, BB8, IG-88, R2) are from the Allende (CV3) chondrite and were cut out of meteorite slices using a diamond saw. After removing any adhering matrix material, pieces of ~0.1–0.5 g were thoroughly cleaned by polishing with SiC and sonication in ethanol, then ground to a fine powder in an agate mortar. Bulk CAI samples as well as terrestrial rock standards were digested in Savillex® vials on a hotplate using HF–HNO_3–$HClO_4$ (2:1:0.02) at 180–200 °C (14 days), followed by inverse aqua regia (2:1 HNO_3–HCl) at 130–150 °C (7 days). After repeated dry-downs with 6 M HCl–0.06 M HF, the samples were completely dissolved in 30–40 ml 6 M HCl–0.06 M HF and small aliquots were taken to determine the rare earth element (REE) patterns (~1–2%) as well as Hf and W concentrations (~1–9%). The chemical separation and isotope measurements of W and Mo followed the protocols described in previous publications (e.g. *33, 35*).

Chemical separation and isotope measurement of W

The aliquots (equivalent to ~1–11 ng W and ~0.5–10 ng Hf) taken to determine Hf and W concentrations by isotope dilution (ID) were spiked with a mixed ^{180}Hf-^{183}W tracer, which was calibrated against pure Hf and W metal standards (*36, 37*). Chemical separation of Hf and W was by anion exchange chromatography (*37*). Typical blanks for the Hf- and W-ID analyses were ~1 pg Hf and ~3 pg W, respectively. The blank corrections for the ID analyses were always <0.3% and are included in the uncertainty of ^{180}Hf/^{184}W, assuming an average uncertainty on the blank correction of 50%.

The separation of W from the unspiked aliquot for isotope composition analyses (IC) was accomplished using a two-stage anion exchange chromatography, slightly modified from previously established procedures (*39*). During the first stage, the samples were loaded in 75 ml 0.5 M HCl–0.5 M HF onto columns filled with 4 ml of pre-cleaned Bio-Rad® AG1-X8 anion exchange resin (200–400 mesh). Most of the sample matrix was washed off the columns with the loading solution and additional 10 ml 0.5 M HCl–0.5 M HF, followed by elution of W in 15 ml 6 M HCl–1 M HF. During the second stage, the samples were dissolved in 6 ml 0.6 M HF–0.4% H_2O_2 and loaded onto Bio-Rad® Poly-Prep columns containing 1 ml of pre-cleaned AG1-X8 resin. The columns were then rinsed with 10 ml 1 M HCl–2% H_2O_2, 9 ml 8 M HCl–0.01 M HF, and 0.5 ml 6 M HCl–1 M HF to remove the high field strength elements (Ti, Zr, Hf, Ta), followed by elution of W with 8.5 ml 6 M HCl–1 M HF. The W cuts from both ion chromatography steps were evaporated at 200°C with added $HClO_4$ to destroy organic compounds. The W yield for this two-column procedure was typically ~70%. Total procedural blanks for the IC measurements were ~20–70 pg W and thus negligible for all samples.

The W isotope measurements were performed on the Thermo Scientific® Neptune *Plus* multi-collector inductively coupled plasma mass spectrometer (MC-ICPMS) in the Institut für Planetologie at the University of Münster and followed the published measurement protocol (*33*). The samples solutions were introduced into the mass spectrometer using a Savillex® C-Flow PFA nebulizer connected to a Cetac® Aridus II desolvator. A combination of (Ni) Jet

sampler and X skimmer cones was used and a total ion beam intensity of ~1.8×10^{-10} A was obtained (in low-resolution mode) for a ~30 ppb W solution at a ~50 µl/min uptake rate. Each analysis consisted of 60 s baseline measurements (deflected beam) followed by 200 isotope ratio measurements of 4.2 s each and consumed ~25 ng of W. Instrumental mass bias was corrected by internal normalization to $^{186}W/^{184}W = 0.92767$ (denoted '6/4') or $^{186}W/^{183}W = 1.98590$ (denoted '6/3') using the exponential law. Possible isobaric interferences of Os on ^{184}W and ^{186}W were monitored by measuring interference-free ^{188}Os and were negligible for all analyzed samples. The W isotope data are reported as ε-unit deviations (*i.e.*, 0.01%) relative to the bracketing Alfa Aesar® solution standards (prepared from a pure W metal, batch no. 22312; refs. *36, 37*). For samples analyzed several times, the reported values represent the mean of pooled solution replicates (Table S2).

The accuracy and precision of the W isotope measurements were assessed by repeated analyses of terrestrial rock standard BHVO-2 (~0.5 g per digestion). Several digestions, which were processed through the full analytical protocol and analyzed together with the samples define an external reproducibility of ~0.1ε (2SD) for all W isotope ratios (Table S5), and the mean $\varepsilon^{182}W$ (6/4) of 0.00±0.11 (2SD, n=12) obtained is indistinguishable from the W isotope composition of the Alfa Aesar standard. As observed in previous high-precision W isotope studies (e.g., *33, 35, 39, 40*), normalizations involving ^{183}W show a small mass-independent effect (~0.1ε) for the processed terrestrial standard. This analytical artifact, which is most likely induced during incomplete dissolution of chemically purified W in Savillex® beakers, is consistent with the nuclear field shift effect and can be accurately corrected (*41*). For the terrestrial standard BHVO-2, this effect was corrected (see *39*, *40*), resulting in W isotope compositions that are indistinguishable from the Alfa Aesar standard and demonstrating that the W isotopic data are accurate within the quoted uncertainty. For the CAI samples investigated here, all $\varepsilon^{i}W$ values involving ^{183}W were corrected using the mean values obtained for the terrestrial standard (see *33*), and all associated uncertainties induced by this correction were propagated into the final uncertainties reported for the W isotope data (Table S2). Most nucleosynthetic W isotope anomalies (*i.e.*, variations in $\varepsilon^{183}W$) we observed are much larger than, and thus clearly resolved from, the small ^{183}W effects observed during mass spectrometric analyses. After correction for the nuclear field shift effect and correction for nucleosynthetic isotope variations, the $\varepsilon^{182}W$ (6/4) and $\varepsilon^{182}W$ (6/3) for each sample agree with each other to within 0.02ε (Table S2).

Chemical separation and isotope measurements of Mo

Molybdenum was collected during the two-stage anion exchange chemistry used for the separation of W following previously established procedures (*35*). During the first stage, Mo largely remained on the resin and was collected (subsequently to the elution of W in 6 M HCl–1 M HF) using 10 ml 3 M HNO_3. A small fraction (~15%) of the Mo is typically eluted together with W, and this Mo was recovered at the end of the second W chemistry, again using (5 ml) 3 M HNO_3 for the Mo elution. The Mo cuts from both W separations were combined, and Mo concentrations for all samples were determined on small aliquots (equivalent to ~2–11 ng Mo) of the combined Mo cuts using a Thermo Scientific® XSeries 2 quadrupole ICPMS in Münster. The subsequent purification of Mo for isotope composition analyses was accomplished using a two-stage ion exchange chromatography modified from published methods (*18*). The samples were loaded in 1 ml 1 M HCl onto columns filled with 1 ml pre-cleaned Eichrom® TRU Resin (100–150 µm) and, after rinsing with 6 ml 1 M HCl, Mo was eluted in 6 ml 0.1 M HCl. This chemistry

was repeated once, but using 7 M HNO_3 and 0.1 M HNO_3 instead of 1 M HCl and 0.1 M HCl. The Mo cuts from all ion chromatography steps were evaporated with added HNO_3 and inverse aqua regia to destroy organic molecules. The Mo yield for the entire procedure was typically ~75%, and total procedural blanks were ~4–5 ng Mo and thus negligible for all samples (*i.e.*, blank corrections were always <0.06ε).

The Mo isotope measurements were performed on the Thermo Scientific® Neptune *Plus* MC-ICPMS in the Institut für Planetologie at the University of Münster and followed a published measurement protocol (*35*). The sample solutions were introduced into the mass spectrometer using a Savillex® C-Flow PFA nebulizer connected to a Cetac® Aridus II desolvator. Typically, a combination of standard (Ni) sampler and H skimmer cones was used and a total ion beam intensity of ~1.1×10^{-10} A was obtained (in low-resolution mode) for a ~100 ppb Mo solution at a ~50 µl/min uptake rate. Each measurement consumed ~80 ng of Mo and consisted of 40 baseline integrations (on-peak zeros) of 8.4 s each, followed by 100 Mo isotope ratio measurements of 8.4 s each. Instrumental mass bias was corrected by internal normalization to $^{98}Mo/^{96}Mo = 1.453173$ (*42*; denoted '8/6') using the exponential law. W used this normalization because it results in large Mo isotope anomalies and distinctive isotope patterns (*18*). Isobaric interferences of Zr and Ru on Mo masses were corrected by monitoring interference-free ^{91}Zr and ^{99}Ru. The final Mo cuts of the samples typically had Ru/Mo and Zr/Mo of <1×10^{-4}, where the interference corrections for Ru (on $\varepsilon^{100}Mo$) and Zr (on $\varepsilon^{94}Mo$) were always <0.5ε and <3ε, respectively. Zr interference corrections of up to ~25ε (Zr/Mo ≈ 1.4×10^{-3}) and Ru interference corrections of >20ε (Ru/Mo ≈ 2.1×10^{-3}) have been previously shown to be accurate to within analytical uncertainty (*35*).

The Mo isotope data are reported as $\varepsilon^{i}Mo$ values (Fig. S2) relative to the mean of bracketing runs of the Alfa Aesar® solution standard, where $\varepsilon^{i}Mo = [(^{i}Mo/^{96}Mo)_{sample} / (^{i}Mo/^{96}Mo)_{standard} - 1] \times 10^4$ (i = 92, 94, 95, 97, 100). For samples analyzed several times, reported values represent the mean of pooled solution replicates (Table S1). The accuracy and precision of the Mo isotope measurements were assessed by repeated analyses of the BHVO-2 standard, several digestions of which were processed through the full analytical protocol and analyzed together with the samples. The $\varepsilon^{i}Mo$ values obtained for the terrestrial rock standard BHVO-2 are indistinguishable from the Alfa Aesar standard, demonstrating that the Mo isotopic data are accurate (Table S6). The external reproducibility of the Mo isotope measurements, as determined by measurements of BHVO-2 run at the same concentrations as the samples ranges from ±0.10 for $\varepsilon^{97}Mo$ to ±0.38 for $\varepsilon^{92}Mo$ (2SD, N=16).

Given the low Mo contents of group II CAIs (~0.6 µg/g), some of these samples (CAI 2a, CAI 12, CAI 17a, CAI 43, 3PO, IG-88) were measured using a combination of standard sampler and X skimmer cones (Table S1). With this setup the total ion beam intensity increases by a factor of ~1.9 compared to the use of an H skimmer cone, allowing us to reach the same intensity (obtained with the standard cone setup) with only half the amount of Mo (*i.e.*, ~40 ng for a single measurement). To evaluate whether the use of an X skimmer cone introduces any systematic shifts in the measured Mo isotope ratios, we performed replicate analyses of the same solutions with both cone setups for the BHVO-2 (BHV29) rock standard and two unfractionated CAIs (BB8, R2), for which sufficient Mo was available and which span a large range of Mo isotope anomalies. The $\varepsilon^{i}Mo$ values obtained for the terrestrial rock standard BHVO-2 are indistinguishable from the Alfa Aesar standard (Table S6) and, as demonstrated in Fig. S6, both cone setups yield indistinguishable Mo isotope signatures for all three samples. This agreement between data obtained using H and X skimmer cones demonstrates that using the high-sensitivity

X skimmer cone neither affects the accuracy of the Mo isotope measurements nor induces any analytical artifacts, even at high precision. For the combination of standard sampler and X skimmer cones, a total ion beam intensity of ~1.0×10^{-10} A was obtained for a ~50 ppb Mo solution at a ~50 µl/min uptake rate, and each measurement consumed ~40 ng of Mo. All other parameters were identical to the measurements with the H skimmer cone. The external reproducibility of the Mo isotope measurements with this cone setup, as determined by repeated measurements of BHVO-2 run at the same intensity as the samples is indistinguishable to the H skimmer analyses and ranges from ±0.13 for ε^{97}Mo to ±0.35 for ε^{92}Mo (2SD, N=15).

In addition to the newly digested CAIs (see above), we obtained Mo isotope data for a set of CAIs (AF01, AF02, AF03, AF04, AI02, AF05, AI01, AI05, AI06, AI07), which were previously investigated for their Hf-W isotope (and REE) systematics (*33*). These samples were processed and measured separately, but the analytical procedures largely followed those described above. These samples were measured at only ~25 ppb using the standard cone setup, resulting in a total ion beam intensity of ~4.5×10^{-11} A. The precision for these analyses was assessed by repeated analyses of the bracketing Alfa Aesar solution standard, yielding an external reproducibility (2SD) of 0.8, 0.6, 0.3, 0.3, and 0.4 for ε^{92}Mo, ε^{94}Mo, ε^{95}Mo, ε^{97}Mo, and ε^{100}Mo, respectively (N=84). For a few samples that contained limited Mo, an unidentified interference on mass 92 meaningfully affected the ε^{92}Mo measurements. For these samples, no ε^{92}Mo data are reported and, as small collateral effects on other isotope ratios cannot be fully excluded, the Δ^{95}Mo values were not considered.

Use of the Δ^{95}Mo notation

Meteoritic samples are mixtures of material derived from a variety of nucleosynthetic sources. Untangling nucleosynthetic dissimilarities can be problematic, particularly distinguishing the difference between a deficit/excess in *s*-process material or an excess/deficit in *r*-process material. Due to the isotope production mechanisms of ^{95}Mo and ^{94}Mo, the Mo isotopes—and particularly the ^{95}Mo-^{94}Mo systematics—can distinguish between sources of nucleosynthetic anomalies. Solar System materials routinely exhibit *s*-process variability in Mo, as established by multiple studies of bulk meteorites (*e.g., 15, 16, 18, 19*), and presolar mainstream silicon carbide (SiC) grains (*e.g.*, *63*). As SiC grains are thought to be produced in the *s*-process of nucleosynthesis in asymptotic giant branch stars, they represent the established *s*-process isotope endmember. The relative percentage of isotopically anomalous SiC grains appears to be the primary cause for isotopic variability in bulk meteorites (*e.g., 18, 43-45*). Since the ε^{95}Mo/ε^{94}Mo slope is well established for bulk meteorites (0.596 [ref. *21*]), and is in agreement with that of presolar mainstream SiC grains (0.59 [ref. *46*]), it is therefore possible to view Mo isotope signatures by subtracting out the *s*-process component (*21*). The formula below defines Δ^{95}Mo notation, indicating parts per million (ppm) variation solely in the *r*-process for the Mo system.

$$\Delta^{95}\text{Mo} \equiv [\varepsilon^{95}\text{Mo} - (0.596 \times \varepsilon^{94}\text{Mo})] \times 100 \qquad \text{Equation S1}$$

Chemical separation and isotope measurements of Ti, Sr, and Ba

Isotopic data not previously reported in the literature were collected using established procedures for chemical separation and isotopic measurement already. For Ti, chemical separation and isotopic measurement followed (*47*) and (*48*). Titanium isotope data were collected using the Neptune *Plus* MC-ICPMS at the Institut für Planetologie and are reported

relative to the OL-Ti reference standard and are mass-bias corrected by internally normalizing to $^{49}Ti/^{47}Ti = 0.749766$.

Chemical isolation and isotopic measurement of Sr followed (*25*). Strontium isotopes were measured on the Triton *Plus* thermal ionization mass spectrometer (TIMS) at the Institut für Planetologie are reported relative to the NBS 987 standard, using $^{86}Sr/^{88}Sr = 0.1194$ for internal normalization. Nucleosynthetic Sr isotope anomalies are expressed as variations in $\varepsilon^{84}Sr$. This is due to the historical use of ^{86}Sr and ^{88}Sr for internal normalization to obtain the radiogenic ^{87}Sr signatures. However, an anomaly in $\varepsilon^{84}Sr$ is simply a product of the chosen normalization scheme and does not necessarily reflect an actual anomaly in the *p*-process isotope ^{84}Sr for CAIs.

Barium separation and isotopic measurement followed (*49*) using the Triton *Plus* TIMS at the Institut für Planetologie. Barium isotopes are reported relative to the SRM 3104a standard using $^{134}Ba/^{136}Ba = 0.3078$ to correct for instrumental fractionation during the measurement.

Rare earth element concentration measurements

The aliquots (equivalent to ~70–240 ng total REE) taken for REE measurements were dissolved in 10 ml 0.5 M HNO_3–0.01 M HF (corresponding to ~250–500 µg sample/ml) and analyzed for their REE concentrations using a Thermo Scientific® XSeries 2 quadrupole in the Institut für Planetologie at the University of Münster. Dissolved aliquots of terrestrial rock standards (BCR-2, BHVO-2, JA-2) were measured at different concentrations and used for calibration. Multiple digestions of BHVO-2 and bulk Allende (CV chondrite) as well as an in-house REE solution standard ('MS REE 2013b') mixed in CI chondritic proportions were run as unknown standards.

The uncertainties of the REE analyses are estimated to be better than 10% (2SD) based on standard runs, and the CI-normalized REE concentration patterns are shown in Fig. S5. The group II CAIs investigated in this study show strongly fractionated 'Group II' REE patterns, which are characterized by a uniform enrichment in light REEs (La to Sm; ~10–40 × CI), variable enrichments/depletions in ultra-refractory REEs (~0.5–20 × CI), and marked enrichments in Tm (~20–30 × CI) relative to other heavy REEs (*32*). In contrast, the two unfractionated CAIs (BB8, R2) display the typical flat 'Group I' pattern with a uniform REE enrichment of ~12 × CI.

Supplementary Text

Nucleosynthetic variation among CAIs: Lithophile elements Ti, Sr, and Ba

For the subset of CAIs additionally investigated for lithophile elements, it is evident that there is limited isotopic variation among CAIs and no distinction can be made between group II or unfractionated (typically igneous) CAIs. A summary of each element (Ti, Sr, and Ba) is given below and methods of measurement are provided in the above section. Nucleosynthetic data are reported using the ε-notation (parts per 10,000 relative to the element's respective standard) using the exponential law to correct for mass bias.

As reported previously, the Ti isotopic compositions of CAIs are slightly variable, but the majority of CAIs show a grouping with excess $\varepsilon^{46}Ti$ of ~1.5 and $\varepsilon^{50}Ti$ of ~9 (*e.g. 29*). Our data for the samples measured are fully consistent with previously reported data for CAIs (*e.g. 29*).

Because Ti isotopes are variable in these samples, we compare with other isotopic variations to search for correlations that may aid in understanding the sources of the isotopic anomalies. For instance, a plot of $\Delta^{95}Mo$ versus $\varepsilon^{50}Ti$ (Fig. 2b; Tables S1;S3) encapsulates many of the geochemical complications in understanding the very early Solar System, but at the same time,

highlights fundamental aspects. ε^{50}Ti is largely uncorrelated with Δ^{95}Mo, indicating that isotopic variability in these two systems have different origins; and because Ti and Mo are cosmochemically dissimilar, could be caused by either: i) dissimilar nucleosynthetic sources of the carrier phases of Mo and Ti, or ii) different processing histories of the carrier phases in the disk. However, like Δ^{95}Mo, ε^{50}Ti variability in CAIs is far greater than anything reported in later-formed Solar System materials. The existence of such a wide range of isotopic anomalies (and *r*-process variation in particular) in CAIs—but not in other Solar System objects—records substantial isotopic heterogeneity and demonstrates that the CAI-forming region sampled a diverse range of precursor materials from the molecular cloud that are unseen in later formed materials.

For Sr, CAIs measured in this study are of multiple petrologic types and exhibit largely homogenous ε^{84}Sr of ~1.1, consistent with previously published studies on bulk CAIs (*12, 25, 50, 51*). When divided into group II and unfractionated groupings, the average anomalies are ε^{84}Sr=1.0 (±0.3) and 1.1(±0.4), respectively, with uncertainty given as the 2SD of the population. Variations in radiogenic Sr (^{87}Sr/^{86}Sr) are greatest in non-igneous CAIs, which have also previously been shown to have consistently higher ^{87}Sr/^{86}Sr than igneous samples (*e.g.*, *12*).

The average ε^{135}Ba and ε^{137}Ba excesses of 0.56 and 0.19 reported here are almost identical to previously published CAI data that average 0.54 (±0.06) and 0.18 (±0.05), respectively, with the 95% CI given for previous data (*12, 52*). Four outliers exist for the Ba isotope system, and these samples exhibit ^{135}Ba anomalies lower than the well-defined average value for CAIs. The slightly lower values in samples AI01, AI02, Bart, and Lisa most likely stem from terrestrial weathering and a mixing of CAI derived Ba and terrestrial Ba incorporated during the samples' time in a hot desert. Influx of terrestrial Ba into meteorites during desert weathering is common (*53*) and has previously been documented for CAIs from other desert meteorites (*25*). As such, the lower than average ^{135}Ba isotopic signatures of these four desert samples are most simply explained by addition of terrestrial Ba to the sample during its time on Earth.

Because many measured samples have similar, yet distinct isotopic compositions from terrestrial standards, in agreement with previous data on a wide range of samples (*12, 25, 52*), it does not appear that secondary alteration has greatly affected most isotopic systems, even for fairly fluid mobile elements such as Sr and Ba. Like Ba, Sr is also particularly mobile in desert environments, and this mobility has reportedly caused issues in previous studies involving CAIs from desert finds (*25*). However, because little, if any, variations exist in the nucleosynthetic Sr, REE, or Hf isotopic signatures of these particular CAIs utilized in this study, it does not appear to be a prominent issue (data shown in Table S2 for the elements and samples measured).

Differences between CAI types

Chemical and petrologic differences between various types of CAIs have been debated extensively in the literature. Diverse nebular conditions and environments of CAI-formation are required to explain their petrology and chemical signatures. This is particularly evident in the trace element distributions in CAIs, pointing to a variety of condensation and evaporation environments in the solar nebula. However, unlike trace elements or petrologic differences that can be created by shifting nebular conditions, unambiguous differences in isotopic signatures between samples reflect differences in the building material of the samples themselves, and not simply the shifting conditions. Whereas there appears to be no discernable isotopic difference between CAI-types based on many lithophile elements as described above, this is not the case for siderophile elements. The group II CAIs vary in both the amount of *s*-, and *r*-process material

incorporated in them compared to Earth (Figure 1a). This dissimilar Mo (and W; Table S3) isotopic signatures of fine-grained (generally "group II") and igneous (generally "unfractionated") CAIs require isotopically dissimilar source material: a difference most easily explained by diverse siderophile carriers among CAI-types.

Secondary alteration

For mobile elements, it is possible that secondary alteration, either on the parent body or in the nebula, may complicate the interpretation of any data derived from CAIs that have seen large amounts of elemental replacement. For most of the samples used in this study of Mo, many other isotopic systems have been investigated, including Ti, Fe, Ni, Sr, Ba, Nd, Sm, Er, Yb, Hf, and W and can assist data interpretation.

Fine-grained, group II CAIs generally have more evidence of alteration than their igneous counterparts (*e.g. 54*), and we consider whether their isotopic signatures are primary. For the fine-grained CAIs of this study, there are large isotopic variations in both Mo (Table S1) and W (Table S2) and determining the role of secondary alteration is necessary, wherever/whenever it may have occurred.

In general, alteration may have caused a previously pristine CAI to inherit the isotopic composition of its surroundings. In this case, alteration of CAIs would cause CAIs to inherit the isotopic signature of the CV3 parent body, or dilute the indigenous CAI signature. CAIs have a higher Mo isotope variability (i.e., ε^{i}Mo anomalies) than other components located in the Allende meteorite. For example, ε^{94}Mo values of the group II CAIs range down to -19, with values less than -9 in three of them (Fig. 1a, Table S1). Resolved Mo isotopic anomalies have been observed for Allende chondrule and matrix separates varying between ~ -2 and +4 in ε^{94}Mo (*16*), and while some fine-grained CAIs do show Mo isotopic signatures that are similar to those of the Allende matrix (*16*), several CAIs show a much larger range of ε^{i}Mo anomalies. Allende matrix, the most likely host of any Mo and W introduced into CAIs during parent body alteration, is characterized by large ε^{183}W deficits (*28*), whereas group II CAI consistently exhibit large and positive ε^{183}W anomalies. Given this, the Mo and W isotope signatures of group II CAIs appear to not be simply sourced from the matrix of their host chondrite during parent body alteration, and the measured CAI signatures are inherent to the CAIs. It is impossible to rule out that some CAIs have been affected, or that the Mo isotopic signatures have been diluted, but it is unlikely that these signatures solely reflect parent body alteration. Alteration is even less likely for igneous CAIs, which contain much higher concentrations of Mo (and W) than the surrounding CV3 matrix.

To further assess potential effects of parent body alteration on the measured nucleosynthetic anomalies, we also obtained Hf-W isotope data for our samples not previously reported in the literature. Other samples that we measured for Mo isotopics produced a Hf-W isochron with the highest initial ^{182}Hf/^{180}Hf measured for material formed in the Solar System (*33*). When anchored to the angrite D'Orbigny (*55, 56*), the initial ^{182}Hf/^{180}Hf of the bulk CAI isochron corresponds to an absolute age of 4567.9±0.7 Ma (*33*), consistent with Pb-Pb ages for CAIs (*6*, *57*). Thus, the bulk CAI isochron defined by these samples provides the initial ^{182}Hf/^{180}Hf of the Solar System, so it seems unlikely that secondary alteration substantially modified the W isotopic compositions of these CAIs. This is because if during alteration, isotopically anomalous W was either added or removed from the CAI, the Hf-W systematics would have been disturbed. Among these samples is the fine-grained group II CAI AF01, which plots precisely on the Hf-W

CAI isochron (Fig. S4) and has a reduced Δ^{95}Mo of ~54, lower than the typical CAI value of ~130 that is characteristic for most unfractionated CAI.

CAIs in our sample that were not analyzed previously (*33*) are plotted in (Fig. S4). The group II CAIs from this sample set appear slightly above the previously established isochron, which is suggestive of disturbance of the Hf-W system. To assess the implication of this observation, we calculated a new isochron regression including all CAIs (i.e., those from (*33*) and the additional CAIs from this study). Owing to the presence of nucleosynthetic W isotope anomalies in CAIs, the isochron regression and correction for nucleosynthetic ^{182}W variations must be done iteratively (see ref. 33). Using the same approach as in (*58*), we obtained the same ε^{182}W– ε^{183}W (for normalization to ^{186}W/^{184}W) and ε^{182}W– ε^{184}W slopes (for normalization to ^{186}W/^{183}W) as in (*33*), indicating that the non-isochronous behavior of some CAIs does not reflect accounted for nucleosynthetic effects. The final isochron regression using the data for all CAIs corrected for nucleosynthetic anomalies yields a slightly shallower slope compared to the original isochron from (*33*) and also displays excess scatter (mean squared weighted deviation; MSWD = 3.2) compared to (*33*) (MSWD = 0.9). Thus, some of the new CAIs from this study seem to have disturbed Hf-W systematics. These CAIs are mainly group II samples with low ^{180}Hf/^{184}W, which plot above the previously established isochron. Owing to the ~8.9 Ma half-life of ^{182}Hf, the timing of this disturbance is difficult to quantify, and so it remains unclear as to whether this disturbance is due to processes in the nebula or on the parent body. Either way, the same CAIs have positive ε^{183}W, unlike the matrix or bulk of their host meteorites. As such, despite the evidence for disturbed Hf-W systematics, the nucleosynthetic W isotope signatures of these samples have not been completely overprinted by parent body processes.

There is evidence for nucleosynthetic isotopic variability within (and between) different CV3 chondrites (compiled for Mo in *16*). Such heterogeneous compositions within a parent body could be from redistribution of elements, such as Mo, from presolar phases such as SiC, which carry an *s*-process signature (ε^{i}Mo) (*59*). However, there is no evidence for *r*-process (Δ^{95}Mo) variability between CV3 meteorites, meaning that different Δ^{95}Mo values of CAIs cannot be explained by parent body alteration on a CV3 chondrite.

Certain elements, such as Fe and Ni, are much less refractory than others investigated and therefore are depleted in CAIs compared to their host chondrites. The Fe isotopic signatures of CAIs—including some of the same samples as our study (Table S2)—cannot be inherited from the parent body as they have different, and highly variable isotopic signatures compared to bulk CV3 meteorites (*60*). Additionally, Ni isotopic signatures from many of these same samples have been reported (*61*). Akin to Fe isotope systematics, Ni isotope patterns in bulk CV3 chondrites are different from CAIs, meaning that the highly variable CAI signatures are not sourced from secondary alteration on the parent body, but contain Ni indigenous to the CAI, regardless of the type of CAI. We find variations in ε^{64}Ni v. Δ^{95}Mo (Fig. S3; Tables S1; S4). The lack of correlation between Δ^{95}Mo and both Ti and Ni is not unexpected, as neither element is expected to be hosted in the same phase as Mo.

Certain forms of alteration are evident for some samples in this data set, again particularly in the fine-grained CAIs; however, depending on the system, the isotopic results can remain robust. Specifically, the highly variable ^{87}Sr/^{86}Sr in the fine-grained CAIs of our samples is evidence of Rb in the samples at variable levels, however, if such an alteration event was the cause of nucleosynthetic variations, there would be a prominent correlation of such anomalies with ^{87}Sr/^{86}Sr, which is not observed. There is no correlation between Δ^{95}Mo and the measured amount of elemental fractionation, as determined by the La/Lu ratio of the samples (Fig. S7).

Fig. S1.

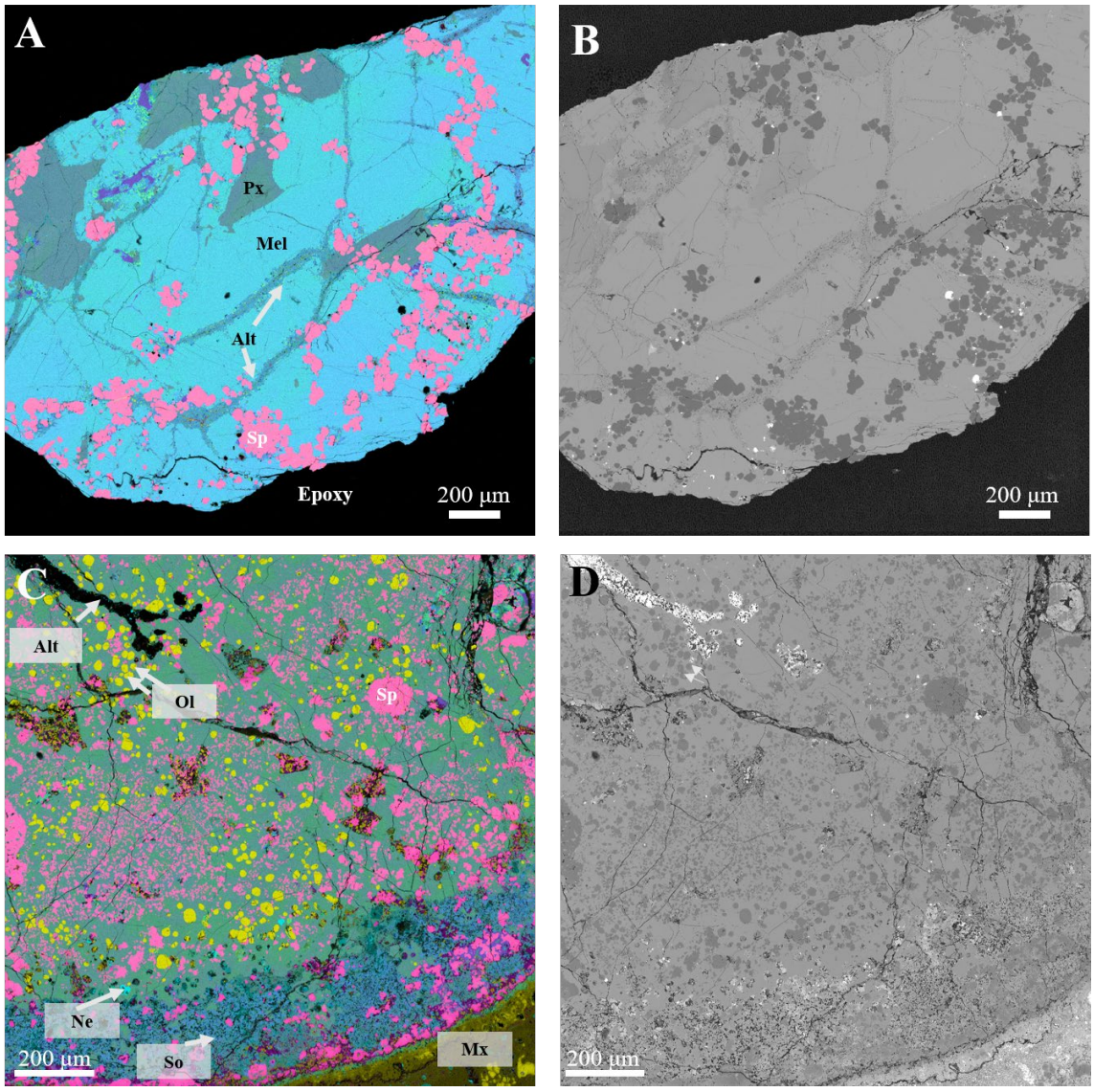

Figure S1: Petrography of two CAIs. (A) False color image (Mg-yellow: Ca-cyan: Al-magenta) of BB8, a coarse-grained Type B CAI showing texture, mineralogy, and alteration features. Typical mineralogy includes melilite (mel), pyroxene (Px), and spinel (Sp). Minor secondary mineralization (Alt) occurs along melilite grain boundaries. (**B**) Backscattered electron image of BB8. (**C**) False color image (Mg-yellow: Ca-cyan: Al-magenta) of R2, a coarse-grained Type B CAI showing texture, mineralogy, and alteration features. Typical mineralogy includes melilite (mel), forsterite olivine (Ol), and spinel (Sp). Secondary mineralogy occurs in cracks and along the object rim and includes nepheline (Ne) and sodalite (So) adjacent to matrix material (Mx). (**D**) Backscattered electron image of R2.

Fig. S2.

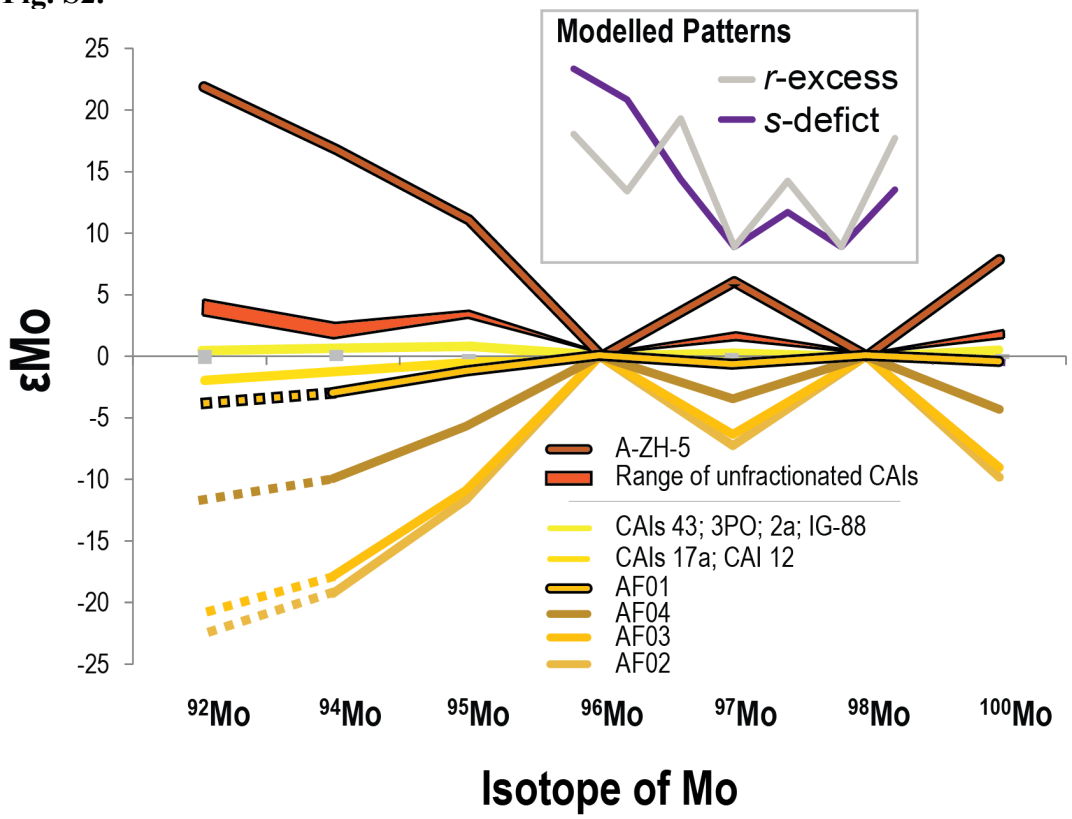

Figure S2: Mo isotope data of CAIs. All samples of this study exhibit isotopic anomalies relative to the terrestrial composition (ε^{i}Mo≡0, where ε-notation designates parts per ten thousand deviation from a terrestrial standard), and from their respective parent bodies. Light gray bars represent 2SD of the terrestrial standard measurements. Group II CAIs, shown in shades of yellow, exhibit substantial s-process variability in Mo isotopes. With the exception of A-ZH-5, the unfractionated CAIs from this and literature sources exhibit limited *s*-process variation. Other than CAI A-ZH-5, literature data (*12, 18, 25*) is contained in the "range" field in orange.

Fig. S3.

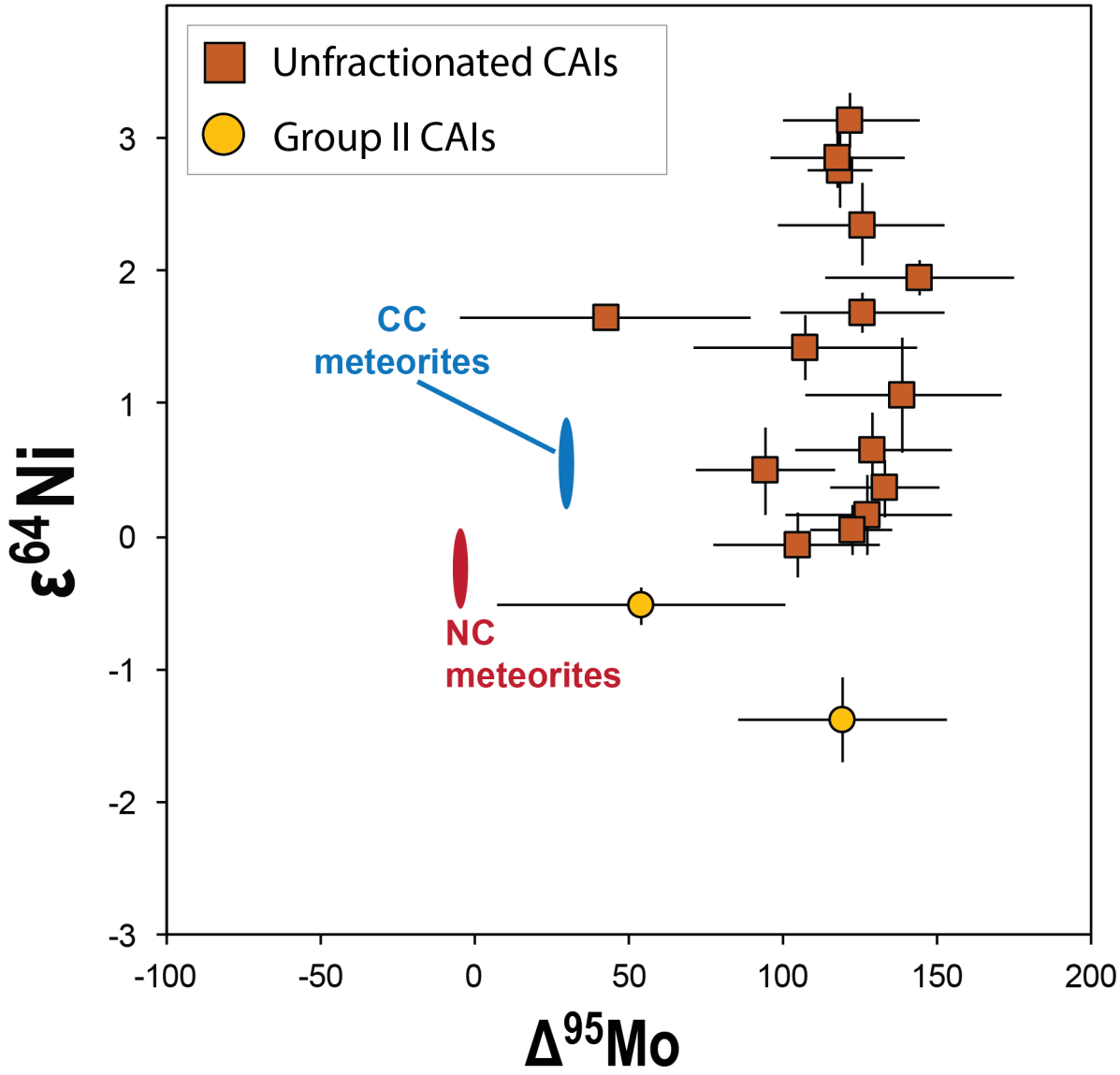

Figure S3: The *r*-process relationship with Ni isotopes. Isotopic anomalies in ε^{64}Ni versus Δ^{95}Mo in our CAI samples. There is no direct correlation between the elements. Nickel data from (*61*) for CAIs and (*44*) and (*22*) for bulk meteorite values. Mo CAI data is from this study, bulk Mo meteorite data is from (*21*).

Fig. S4.

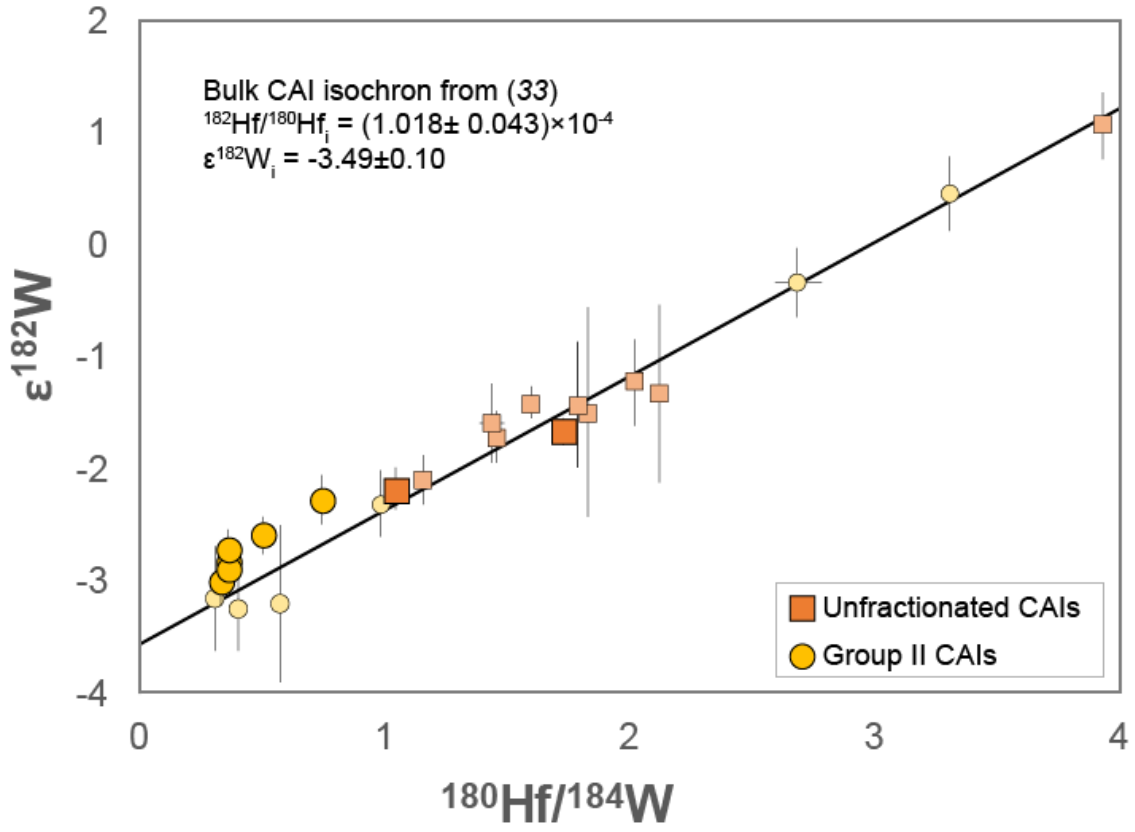

Figure S4: Hf-W chronology of CAIs. Hf-W isochron diagram showing the CAIs for which we obtained Mo isotope data. Lighter symbols represent data from (*38*); bold symbols represent CAIs analyzed for Hf-W systematics in this study, which are broadly consistent with the bulk CAI isochron (solid line) as defined by (*33*). The $\varepsilon^{182}W$ values are normalized to $^{186}W/^{183}W$ and corrected for a small effect of nucleosynthetic anomalies (see Methods).

Fig. S5.

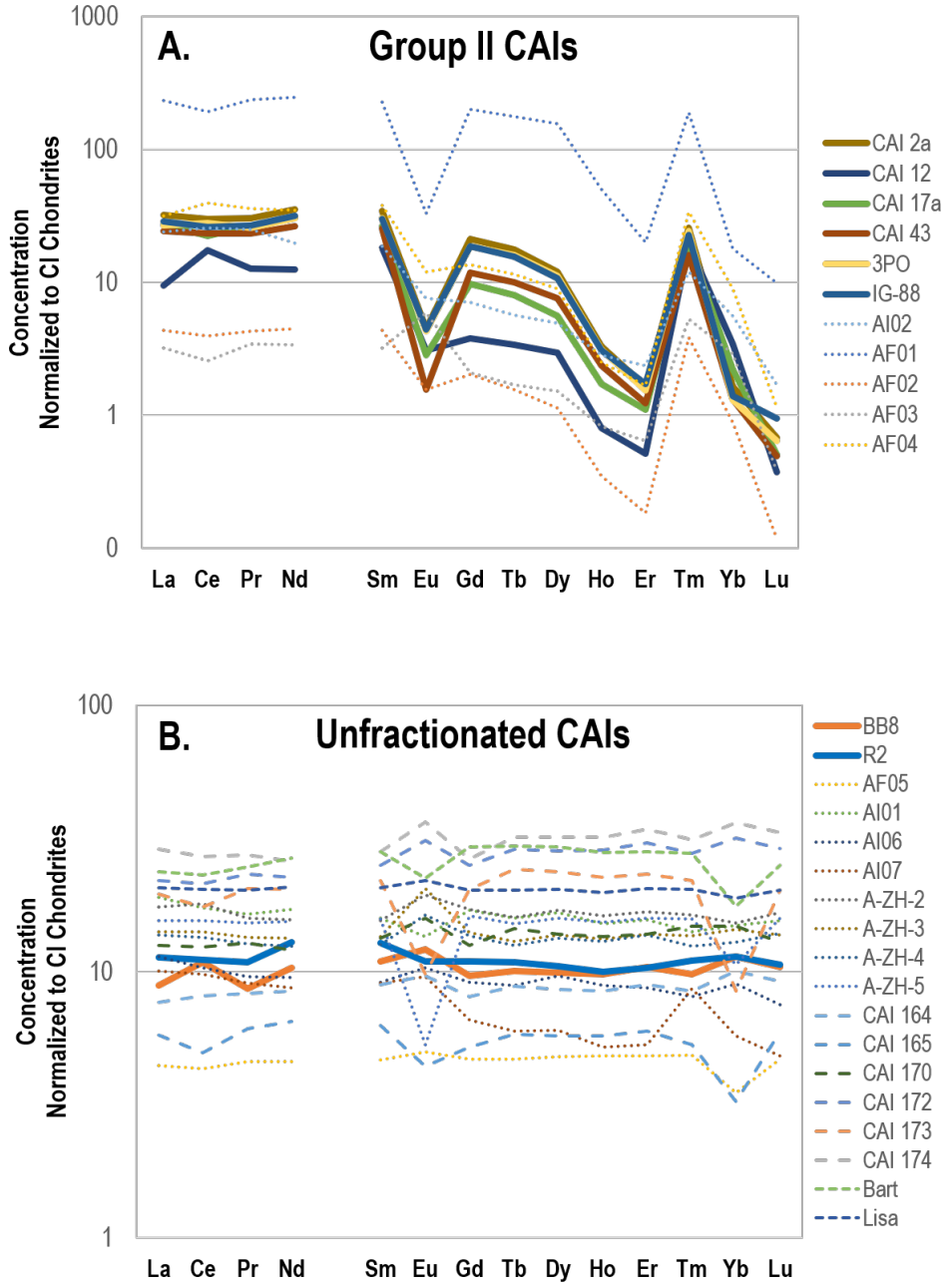

Figure S5: Rare earth element patterns of CAIs. (A) CAIs with group II REE patterns (**B**) CAIs with unfractionated REEs. Data in bold solid colors are newly reported samples, whereas dashed lines are literature data (*25, 33, 34*).

Fig. S6.

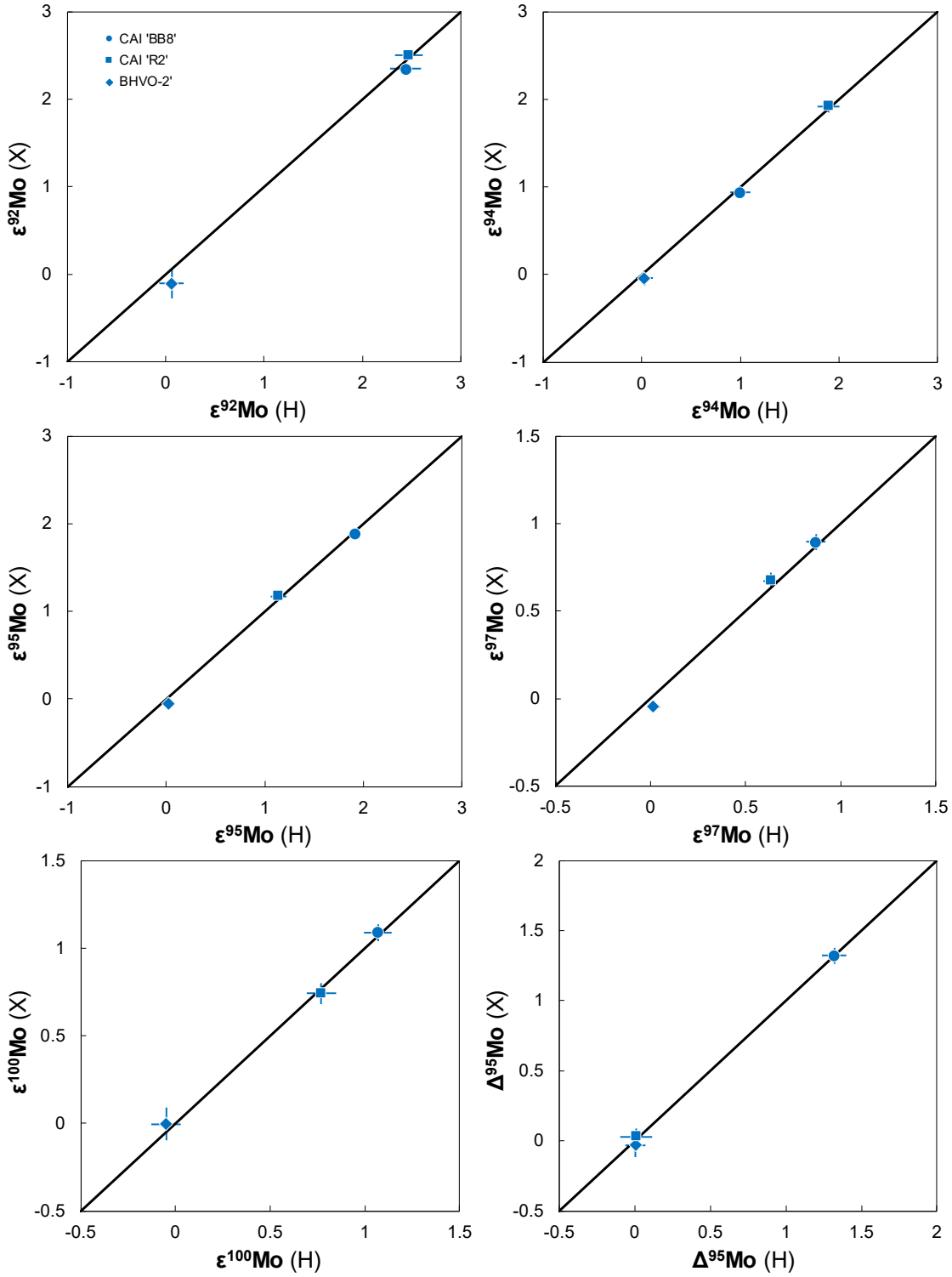

Figure S6: Skimmer cone comparison. Direct comparison of Mo isotope data obtained using H and X skimmer cones (in combination with a standard sampler cone). Mo isotope data for the terrestrial rock standard BHVO-2 and two unfractionated CAIs (BB8, R2) were obtained on the same solutions. Solid bold lines are slope=1.

Fig. S7

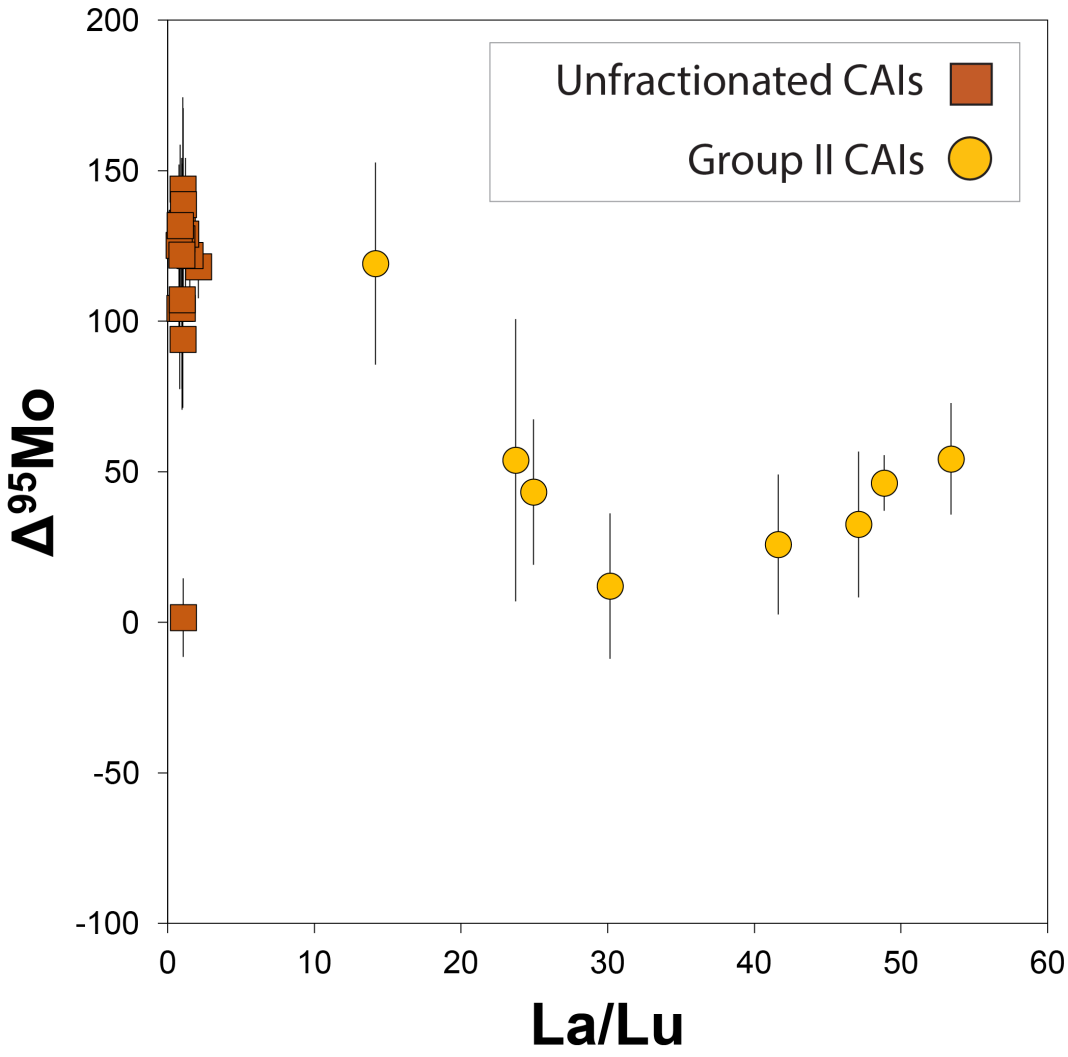

Figure S7: Elemental fractionation and *r*-process components in CAIs. The Δ^{95}Mo of CAIs of this study plotted against the chondrite normalized La/Lu ratio. There is no correlation between Mo isotope data with the amount of elemental fractionation in the CAI.

Table S1: CAI isotopics and data table. Sample name, type (Group II "GII" or unfractionated "UF": fine-grained samples are designated by "fg" the group "Gx" of CAI is given, if known), mass (in mg), type of cone used for measurement (H, X), number of times each sample was measured (N), La/Lu (CI-normalized), Mo concentration (in ng/g), and Mo isotopics of CV3 CAIs measured in this and previous studies. All ε-values are calculated after internal normalization to $^{98}Mo/^{96}Mo$=1.453173 (*42*). Uncertainties (±) are 95% confidence interval when samples are measured >3 times, or the 2SD of the standard, whichever is larger. Mo concentrations as determined by quadrupole ICP-MS, which have an uncertainty of ~5%. With the exception of AI01 (NWA 6870) and AI02 (NWA 6717), samples of this study were removed from the Allende meteorite. CAI data from Bart and Lisa from (*25*) were removed from meteorites NWA 6254 and NWA 6991, respectively.

Sample	Type	Mass (mg)	Cone	N	La/Lu	[Mo] µg/g	$\varepsilon^{92}Mo$	±	$\varepsilon^{94}Mo$	±	$\varepsilon^{95}Mo$	±	$\varepsilon^{97}Mo$	±	$\varepsilon^{100}Mo$	±	$\Delta^{95}Mo$	±
AF01	GII (fg)	289	H	1	23.7	0.37	-	-	-3.0	0.6	-1.3	0.3	-0.7	0.3	-0.5	0.4	54	47
AF02	GII (fg)	120	H	2	36.9	-	-	-	-19.3	0.6	-11.6	0.3	-7.3	0.3	-9.8	0.4	-	-
AF03	GII (fg)	34	H	1	8.4	-	-	-	-17.9	0.6	-10.9	0.3	-6.3	0.3	-9.0	0.4	-	-
AF04	GII (fg)	288	H	3	27.5	-	-	-	-9.9	0.7	-5.7	0.5	-3.5	0.3	-4.3	0.6	-	-
CAI 17a	GII (fg)	419	X	4	51.9	0.53	0.65	0.21	0.26	0.25	0.70	0.11	0.36	0.09	0.38	0.12	54	21
CAI 12	GII (fg)	136	X	1	24.2	0.56	0.31	0.35	-0.02	0.25	0.42	0.19	0.21	0.13	0.01	0.23	43	26
CAI 43	GII (fg)	511	X	5	47.4	0.63	-3.22	0.19	-2.80	0.14	-1.20	0.04	-0.63	0.06	-0.91	0.07	46	9
3PO	GII (fg)	368	X	4	40.4	0.62	-0.85	0.15	-0.67	0.25	-0.14	0.18	-0.09	0.13	-0.36	0.17	26	23
CAI 2a	GII (fg)	268	X	3	45.7	0.63	-1.95	0.35	-1.71	0.25	-0.69	0.19	-0.36	0.13	-0.74	0.23	32	26
IG-88	GII (fg)	117	X	1	29.3	0.71	-0.73	0.35	-0.70	0.25	-0.29	0.19	-0.13	0.13	-0.26	0.23	12	26
AI02	GII	103	H	5	14.2	500	3.1	0.6	1.0	0.3	1.8	0.3	0.8	0.2	1.0	0.2	119	34
BB8	UF (GI)	512	H	10	0.8	16.34	2.43	0.16	1.00	0.10	1.92	0.05	0.87	0.05	1.07	0.07	132	9
BB8 (rep.)			X	10			2.35	0.07	0.94	0.06	1.88	0.04	0.90	0.05	1.09	0.05	132	5
R2	UF (GI)	512	H	10	1.0	8.63	2.47	0.14	1.90	0.11	1.14	0.08	0.63	0.04	0.77	0.08	2	13
R2 (rep.)			X	10			2.50	0.05	1.92	0.07	1.17	0.04	0.67	0.04	0.74	0.06	3	6
AF05	UF (GI)	69	H	3	0.9	7.60	3.3	0.8	1.5	0.2	2.1	0.2	0.9	0.1	1.2	0.6	122	19
AI01	UF (GI)	82	H	4	1.2	6.24	3.0	0.7	0.8	0.3	1.8	0.2	0.5	0.2	0.8	0.1	129	25
AI05	UF	77	H	2	-	1.02	-	-	1.4	0.6	1.3	0.3	0.3	0.3	0.7	0.4	42	47
AI06	UF (GI)	168	H	7	1.5	28.77	3.0	0.2	1.4	0.2	2.0	0.2	0.9	0.1	1.0	0.1	122	22
AI07	UF (GI)	137	H	6	2.1	5.78	-	-	1.7	0.2	2.2	0.1	0.9	0.1	1.1	0.1	118	10
A-ZH-1*	UF	120	H	5	-	8.27	2.8	0.2	1.3	0.3	2.0	0.1	0.8	0.1	1.1	0.1	118	22
A-ZH-2*	UF (G1)	180	H	4	1.1	7.89	2.4	0.6	1.0	0.5	2.0	0.1	1.1	0.2	1.3	0.3	139	32
A-ZH-3*	UF (GI)	70	H	2	1.0	6.59	2.2	0.5	0.7	0.4	1.9	0.2	0.9	0.2	0.9	0.3	144	30
A-ZH-4*	UF (GI)	200	H	5	1.0	6.75	3.1	0.4	1.5	0.2	2.2	0.1	1.1	0.1	1.2	0.3	133	18
A-ZH-5*	UF (GIII)	90	H	1	1.0	5.78	21.9	0.7	16.8	0.4	11.1	0.3	6.1	0.2	7.8	0.4	107	37
A-ZH-10*	UF	234	H	10	-	2.15	3.2	0.5	1.6	0.2	2.1	0.2	0.9	0.1	1.1	0.3	110	27
CAI 164†	UF (GI)	705	H	4	0.8	6.56	2.4	0.4	1.2	0.3	1.8	0.2	0.7	0.2	1.2	0.3	104	28
CAI 165†	UF (GIII)	2838	H	3	1.0	2.31	2.7	0.4	1.2	0.3	2.0	0.2	0.8	0.2	1.1	0.3	126	37
CAI 170†	UF (GI)	199	H	1	1.0	7.39	2.8	0.4	1.6	0.3	2.0	0.2	0.8	0.2	2.1	0.3	104	34
CAI 172†	UF (GI)	441	H	3	0.8	6.14	3.0	0.4	1.3	0.3	2.0	0.2	0.9	0.2	1.5	0.3	126	31
CAI 173†	UF (GIII)	607	H	3	1.0	5.17	2.9	0.4	1.3	0.3	2.1	0.2	0.9	0.2	1.3	0.3	127	40
CAI 174*	UF (GI)	441	H	3	0.9	6.02	2.7	0.4	0.9	0.3	1.9	0.2	0.9	0.2	1.5	0.3	132	47
Bart‡	UF (GIII)	69	H	6	0.9	20.48	2.8	0.3	1.4	0.2	2.0	0.1	0.9	0.1	1.2	0.1	122	13
Lisa‡	UF (GV)	53	H	3	1.0	1.63	1.8	0.4	0.8	0.3	1.4	0.2	0.7	0.1	0.8	0.2	94	23

* Data from (*18*)
† Data from (*12*)
‡ Data from (*25*)

Table S2. Hf-W isotope data for bulk CAIs investigated in this study. Given uncertainties are based on the external reproducibility (2SD) obtained from repeated analyses of the terrestrial standard (Table S5) or the in-run error (2SE), whichever is larger. For samples with N>3, the uncertainties represent 95% confidence intervals (95% CI). Samples "CAI 12" and "IG-88" were run at slightly lower intensities (12 ppb instead of 30 ppb), as reflected by their larger uncertainties. The final uncertainties include all propagated uncertainties induced by the correction for a small mass-independent effect on ^{183}W as well as by the correction for ^{182}Hf decay ($\varepsilon^{182}W_i$) using $(^{182}Hf/^{180}Hf)_i = (1.018\pm0.043)\times10^{-4}$ (*58*) or nucleosynthetic isotope anomalies ($\varepsilon^{182}W_{nuc.\ corr.}$). The latter were corrected according to (*i*) $\varepsilon^{182}W\ (6/4)_{nuc.\ corr.} = \varepsilon^{182}W\ (6/4)_{meas.} - (1.41\pm0.06) \times \varepsilon^{183}W\ (6/4)$ and (*ii*) $\varepsilon^{182}W\ (6/3)_{nuc.\ corr.} = \varepsilon^{182}W\ (6/3)_{meas.} + (0.11\pm0.05) \times \varepsilon^{184}W\ (6/3)$ (*58*). N: number of analyses.

Sample	Hf (ng/g)	W (ng/g)	$^{180}Hf/^{184}W$ (± 2σ)	N (W-IC)	$\varepsilon^{182}W_{meas.}$ (± 2σ)	$\varepsilon^{183}W$ (± 2σ)	$\varepsilon^{182}W_i$ (± 2σ)	$\varepsilon^{182}W_{nuc.\ corr.}$ (± 2σ)	$\varepsilon^{182}W_{meas.}$ (± 2σ)	$\varepsilon^{184}W$ (± 2σ)	$\varepsilon^{182}W_i$ (± 2σ)	$\varepsilon^{182}W_{nuc.\ corr.}$ (± 2σ)
					normalized to $^{186}W/^{184}W = 0.92767$ ('6/4')				normalized to $^{186}W/^{183}W = 1.98590$ ('6/3')			
Group II CAIs												
CAI 17a	42	98	0.501 ± 0.002	1	-0.93 ± 0.11	1.18 ± 0.15	-1.52 ± 0.11	-2.59 ± 0.24	-2.50 ± 0.16	-0.79 ± 0.10	-3.09 ± 0.16	-2.59 ± 0.16
CAI 12	35	125	0.334 ± 0.002	1	-0.78 ± 0.34	1.56 ± 0.23	-1.18 ± 0.34	-2.99 ± 0.48	-2.87 ± 0.20	-1.04 ± 0.15	-3.27 ± 0.20	-2.99 ± 0.21
CAI 43	36	116	0.369 ± 0.001	1	-0.80 ± 0.11	1.44 ± 0.14	-1.23 ± 0.11	-2.82 ± 0.24	-2.71 ± 0.15	-0.96 ± 0.09	-3.15 ± 0.15	-2.82 ± 0.16
3PO	35	114	0.368 ± 0.001	1	0.41 ± 0.11	2.34 ± 0.15	-0.02 ± 0.11	-2.89 ± 0.27	-2.71 ± 0.16	-1.56 ± 0.10	-3.14 ± 0.16	-2.88 ± 0.18
CAI 2a	35	113	0.363 ± 0.001	1	0.37 ± 0.12	2.22 ± 0.16	-0.06 ± 0.12	-2.77 ± 0.28	-2.60 ± 0.17	-1.48 ± 0.10	-3.02 ± 0.17	-2.76 ± 0.18
IG-88	77	121	0.748 ± 0.002	1	0.13 ± 0.34	1.71 ± 0.23	-0.75 ± 0.34	-2.29 ± 0.48	-2.14 ± 0.21	-1.14 ± 0.15	-3.02 ± 0.21	-2.27 ± 0.22
Unfractionated CAIs												
BB8	1898	2132	1.050 ± 0.003	6	-2.18 ± 0.04	0.00 ± 0.13	-3.42 ± 0.07	-2.18 ± 0.18	-2.17 ± 0.14	0.00 ± 0.08	-3.41 ± 0.15	-2.17 ± 0.14
R2	1554	1059	1.732 ± 0.004	6	-1.43 ± 0.02	0.18 ± 0.12	-3.46 ± 0.09	-1.68 ± 0.17	-1.66 ± 0.13	-0.12 ± 0.08	-3.70 ± 0.16	-1.67 ± 0.13

Table S3: Titanium isotope compositions. Isotopic values of Ti for samples of this study.

CAI	ε^{46}Ti	±	ε^{48}Ti	±	ε^{50}Ti	±
3PO	2.06	0.13	0.36	0.05	12.04	0.16
AF01	1.82	0.15	0.21	0.45	9.14	0.12
AF02	1.96	0.12	0.17	0.20	11.82	0.25
AF03	2.05	0.29	0.19	0.20	11.57	0.26
AF04	1.31	0.09	0.32	0.17	8.38	0.14
AI02	1.70	0.13	0.42	0.11	8.85	0.20
CAI 12	1.69	0.14	0.55	0.12	9.14	0.12
CAI 17a	1.82	0.12	0.60	0.09	9.53	0.14
CAI 2a	2.01	0.16	0.39	0.08	12.14	0.12
CAI 43	1.82	0.11	0.60	0.11	8.96	0.14
IG-88	2.03	0.13	0.39	0.05	11.70	0.15
AF05	1.80	0.14	0.35	0.10	9.40	0.09
AI01	1.61	0.03	0.28	0.48	9.29	0.15
AI05	1.49	0.03	0.16	0.23	8.23	0.09
AI06	1.55	0.14	0.32	0.28	9.35	0.13
AI07	1.64	0.05	-0.22	0.27	9.35	0.12
A-ZH-1	1.55	0.11	0.49	0.06	9.12	0.13
A-ZH-2	1.60	0.07	0.53	0.04	9.38	0.11
A-ZH-3	1.73	0.50	0.39	0.14	9.38	0.47
A-ZH-4	1.48	0.06	0.50	0.05	9.31	0.09
A-ZH-5	1.57	0.10	0.51	0.04	9.51	0.07
R2	0.27	0.14	0.16	0.07	2.89	0.16
BB8	1.92	0.06	0.57	0.11	9.50	0.11
CAI 164*	1.48	0.17	0.43	0.08	9.19	0.22
CAI 165*	1.80	0.17	0.37	0.07	9.20	0.20
CAI 170*	1.98	0.17	0.44	0.18	9.70	0.22
CAI 172*	1.64	0.17	0.35	0.07	9.55	0.17
CAI 173*	1.56	0.17	0.31	0.12	9.11	0.25
CAI 174*	1.62	0.17	0.36	0.07	9.06	0.17
Lisa*	1.68	0.17	0.48	0.15	9.43	0.17
Bart*	1.60	0.17	0.47	0.14	9.37	0.19

* Data from (*63*)

Table S4: Isotopic anomalies in multiple elements. Isotopic values of other elemental system for some samples of this study. Only one isotope of each system is shown. References are given at the top of the column, where "TS" denotes this study. The average uncertainty for each isotope measured is given at the bottom.

Primary ref.	*60*	*61*	*12, 25, TS*	*12, 25, TS*	*12, TS*	*12, 45*	*12, 45*	*60*	*60*	*60*
CAI	δ^{56}Fe	ε^{64}Ni	ε^{84}Sr	^{87}Sr/^{86}Sr	ε^{135}Ba	ε^{145}Nd	ε^{148}Sm	ε^{170}Er	ε^{176}Yb	ε^{180}Hf
AF01	-1.25	-0.52	0.73	0.704516	0.62					
AF02	-0.44	-0.54	1.07	0.746798	0.67					
AF03	-0.46	0.36	1.00	0.723235	0.68					
AF04	-0.45	0.29	1.10	0.762930	0.49					
AI02	-0.52	-1.38	1.04	0.701176	0.20					
AF05			1.17	0.699328	0.55					
AI01	0.15	0.66	0.99	0.703480	0.26					0.35
AI05		1.64	0.84	0.699428	0.53					
AI06		3.14	1.05	0.699615	0.61					0.31
AI07		2.76	1.21	0.699144	0.62					0.39
A-ZH-1	1.29	2.85	1.44	0.700674						
A-ZH-2	-0.86	1.07	1.18	0.699478					-0.75	
A-ZH-3	-0.38	1.95								
A-ZH-4	-0.61	0.36	1.39	0.699821				-0.07		
A-ZH-5	-0.46	1.42	1.07	0.718868		-0.19	0.62			
Bart	-1.03	0.05	0.44	0.699617	0.40	-0.23	0.50	-0.14		
CAI 164	-0.84	-0.06	1.30	0.700866	0.59	-0.25	0.54	-0.18	-0.58	0.28
CAI 165		1.69	0.95	0.699570	0.57	-0.25	0.54	-0.22	-0.51	0.33
CAI 168	0.44	1.75	1.50	0.699234	0.57	-0.16	0.64	-0.24	-0.58	0.29
CAI 170	-0.04		1.70	0.699502	0.56	-0.23	0.59	0.01	-0.58	
CAI 171	-0.47	0.09	1.25	0.702016	0.61	-0.19	0.65	-0.31		
CAI 172	0.38	2.35	1.50	0.699344	0.59	-0.18	0.60	-0.13	-0.54	0.31
CAI 173	-0.58	0.17	1.30	0.701662	0.47	-0.21	0.57	-0.09		0.26
CAI 174	0.43		1.50	0.699403	0.53	-0.34	0.55	-0.19	-0.56	0.28
Lisa	0.18	0.5	1.40	0.699419	0.41	-0.25	0.58	-0.17		
Ave. 2SD	0.05	0.27	0.5	0.000010	0.08	0.09	0.17	0.11	0.1	0.09

Table S5: Basalt standard data for Hf-W. Hf-W isotope data for the terrestrial rock standard BHVO-2. Three separate digestions (~0.5 g material) were processed through the full chemical separation procedure and analyzed with each set of samples and are designated by BVH26, BHV27, and BHV28. Each line represents a single measurement, which consumed ~25 ng of W (run at ~30 ppb).

ID	Hf (ng/g)	W (ng/g)	$\varepsilon^{182}W_{meas.}$ (± 2 s.e.)	$\varepsilon^{183}W_{meas.}$ (± 2 s.e.)	$\varepsilon^{183}W_{corr.}$* (± 2σ)	$\varepsilon^{182}W_{meas.}$ (± 2 s.e.)	$\varepsilon^{182}W_{corr.}$* (± 2σ)	$\varepsilon^{184}W_{meas.}$ (± 2 s.e.)	$\varepsilon^{184}W_{corr.}$* (± 2σ)
			normalized to $^{186}W/^{184}W = 0.92767$			normalized to $^{186}W/^{183}W = 1.98590$			
BHV26.1	4588	218	0.10 ± 0.09	-0.07 ± 0.08	0.06 ± 0.10	0.17 ± 0.08	0.08 ± 0.13	0.05 ± 0.05	-0.04 ± 0.07
BHV26.2	–	–	-0.03 ± 0.08	-0.07 ± 0.08	-0.02 ± 0.10	0.07 ± 0.08	-0.02 ± 0.13	0.05 ± 0.05	0.01 ± 0.07
BHV26.3	–	–	-0.04 ± 0.09	-0.09 ± 0.08	0.01 ± 0.10	0.13 ± 0.07	0.01 ± 0.12	0.06 ± 0.05	0.00 ± 0.06
BHV27.1	4420	211	0.02 ± 0.10	-0.11 ± 0.09	0.01 ± 0.11	0.15 ± 0.09	0.01 ± 0.15	0.07 ± 0.06	-0.01 ± 0.08
BHV27.2	–	–	0.04 ± 0.09	-0.14 ± 0.08	0.04 ± 0.11	0.23 ± 0.09	0.05 ± 0.14	0.09 ± 0.05	-0.02 ± 0.07
BHV27.3	–	–	-0.04 ± 0.10	-0.20 ± 0.09	-0.02 ± 0.12	0.23 ± 0.10	-0.03 ± 0.15	0.13 ± 0.06	0.01 ± 0.08
BHV28.1	4488	214	0.03 ± 0.11	-0.07 ± 0.10	0.03 ± 0.12	0.12 ± 0.09	0.03 ± 0.15	0.04 ± 0.07	-0.02 ± 0.08
BHV28.2	–	–	0.04 ± 0.09	-0.14 ± 0.08	0.02 ± 0.10	0.20 ± 0.09	0.02 ± 0.13	0.09 ± 0.05	-0.01 ± 0.07
BHV28.3	–	–	-0.07 ± 0.10	-0.24 ± 0.09	-0.05 ± 0.11	0.25 ± 0.09	-0.07 ± 0.14	0.16 ± 0.06	0.03 ± 0.07
BHV29.1	4509	215	-0.07 ± 0.10	-0.17 ± 0.08	-0.05 ± 0.11	0.15 ± 0.09	-0.07 ± 0.14	0.11 ± 0.06	0.03 ± 0.07
BHV29.2	–	–	0.01 ± 0.09	-0.08 ± 0.09	0.01 ± 0.10	0.11 ± 0.08	0.01 ± 0.14	0.05 ± 0.06	-0.01 ± 0.07
BHV29.3	–	–	-0.05 ± 0.09	-0.07 ± 0.08	-0.03 ± 0.10	0.06 ± 0.08	-0.04 ± 0.13	0.05 ± 0.05	0.02 ± 0.07
N	4	4	12	12	12	12	12	12	12
Mean	4501	215	0.00	-0.12	0.00	0.16	0.00	0.08	0.00
2 s.d.	138	6.0	0.11	0.12	0.07	0.12	0.09	0.08	0.05
95% CI	110	4.8	0.03	0.04	0.02	0.04	0.03	0.02	0.01

* Corrected for a small mass-independent effect on ^{183}W (*39, 40*); uncertainties on corrected $\varepsilon^{i}W$ values include all propagated uncertainties induced by the correction.

Table S6: Skimmer cone comparison. Mo isotope data for the terrestrial rock standard BHVO-2. This includes three separate digestions (~0.5 g material) that were processed through the full chemical separation procedure and analyzed with each set of samples (BHV22, BHV28, BHV29). Each line represents a single measurement, which consumed ~80 ng of Mo (run at ~100 ppb) for the H skimmer cone setup and ~40 ng of Mo (run at ~50 ppb) for the X skimmer cone setup.

ID	ε^{92}Mo (± 2 s.e.)	ε^{94}Mo (± 2 s.e.)	ε^{95}Mo (± 2 s.e.)	ε^{97}Mo (± 2 s.e.)	ε^{100}Mo (± 2 s.e.)
Measured with H skimmer cone					
BHV28.1	-0.11 ± 0.16	-0.01 ± 0.13	-0.02 ± 0.09	0.03 ± 0.07	-0.01 ± 0.10
BHV28.2	0.11 ± 0.19	0.10 ± 0.14	0.10 ± 0.09	0.11 ± 0.07	-0.12 ± 0.12
BHV28.3	-0.27 ± 0.19	-0.05 ± 0.14	-0.01 ± 0.11	-0.04 ± 0.09	0.00 ± 0.11
BHV28.4	-0.21 ± 0.21	-0.02 ± 0.14	-0.06 ± 0.10	0.00 ± 0.08	0.06 ± 0.12
BHV28.5	-0.45 ± 0.20	-0.24 ± 0.14	-0.14 ± 0.10	-0.06 ± 0.09	0.06 ± 0.14
BHV28.6	0.01 ± 0.22	0.08 ± 0.16	0.13 ± 0.12	-0.06 ± 0.08	-0.14 ± 0.13
BHV28.7	-0.20 ± 0.19	-0.25 ± 0.14	-0.11 ± 0.09	-0.05 ± 0.08	0.11 ± 0.12
BHV28.8	-0.18 ± 0.21	-0.10 ± 0.12	-0.02 ± 0.10	0.04 ± 0.09	-0.08 ± 0.12
BHV29.1	0.05 ± 0.19	0.06 ± 0.14	-0.01 ± 0.10	-0.01 ± 0.07	-0.07 ± 0.13
BHV29.2	-0.13 ± 0.20	-0.08 ± 0.15	-0.01 ± 0.12	0.02 ± 0.08	-0.10 ± 0.15
BHV29.3	0.06 ± 0.22	0.03 ± 0.17	-0.04 ± 0.10	-0.02 ± 0.09	0.06 ± 0.13
BHV29.4	-0.04 ± 0.22	-0.05 ± 0.15	0.07 ± 0.10	0.03 ± 0.08	-0.23 ± 0.13
BHV29.5	-0.10 ± 0.21	-0.10 ± 0.16	-0.03 ± 0.11	-0.03 ± 0.08	0.05 ± 0.14
BHV29.6	0.23 ± 0.21	0.21 ± 0.14	0.00 ± 0.10	0.09 ± 0.09	-0.06 ± 0.13
BHV29.7	0.21 ± 0.20	0.06 ± 0.15	0.10 ± 0.10	0.00 ± 0.09	-0.03 ± 0.15
BHV29.8	0.21 ± 0.23	0.06 ± 0.14	0.08 ± 0.10	0.05 ± 0.08	-0.01 ± 0.15
N	16	16	16	16	16
Mean	-0.05	-0.02	0.00	0.01	-0.03
2 s.d.	0.38	0.24	0.15	0.10	0.18
95% CI	0.10	0.06	0.04	0.03	0.05
Measured with X skimmer cone					
BHV22.X1	-0.06 ± 0.20	0.10 ± 0.17	0.01 ± 0.11	-0.09 ± 0.08	0.07 ± 0.12
BHV22.X2	0.11 ± 0.19	0.10 ± 0.12	0.06 ± 0.11	0.05 ± 0.08	0.04 ± 0.13
BHV22.X3	0.15 ± 0.17	0.07 ± 0.14	0.16 ± 0.10	0.11 ± 0.08	-0.06 ± 0.13
BHV22.X4	0.00 ± 0.18	-0.23 ± 0.14	-0.05 ± 0.10	0.04 ± 0.07	-0.06 ± 0.13
BHV22.X5	-0.15 ± 0.20	-0.03 ± 0.14	-0.05 ± 0.11	0.04 ± 0.08	-0.05 ± 0.12
BHV29.X1	0.22 ± 0.20	0.09 ± 0.14	0.10 ± 0.10	-0.01 ± 0.08	-0.16 ± 0.12
BHV29.X3	-0.12 ± 0.21	-0.02 ± 0.15	-0.12 ± 0.10	0.00 ± 0.09	-0.06 ± 0.12
BHV29.X4	0.09 ± 0.20	0.08 ± 0.17	0.03 ± 0.11	-0.07 ± 0.09	0.14 ± 0.13
BHV29.X5	-0.14 ± 0.22	0.05 ± 0.17	0.01 ± 0.12	-0.03 ± 0.08	0.13 ± 0.13
BHV29.X6	0.05 ± 0.24	0.02 ± 0.18	0.01 ± 0.12	-0.01 ± 0.09	-0.04 ± 0.14
BHV29.X7	-0.28 ± 0.21	-0.11 ± 0.15	-0.20 ± 0.11	-0.13 ± 0.08	0.06 ± 0.16
BHV29.X8	0.04 ± 0.21	0.03 ± 0.14	-0.04 ± 0.11	-0.07 ± 0.09	-0.22 ± 0.12
BHV29.X9	-0.43 ± 0.21	-0.34 ± 0.15	-0.18 ± 0.09	-0.09 ± 0.09	0.08 ± 0.12
BHV29.X10	-0.13 ± 0.22	-0.05 ± 0.15	-0.05 ± 0.11	-0.03 ± 0.09	0.09 ± 0.12
BHV29.X11	0.12 ± 0.22	0.01 ± 0.14	0.02 ± 0.11	-0.07 ± 0.08	-0.19 ± 0.15
N	15	15	15	15	15
Mean	-0.04	-0.01	-0.02	-0.02	-0.01
2 s.d.	0.35	0.25	0.19	0.13	0.23
95% CI	0.10	0.07	0.05	0.04	0.06

References and Notes

1. J. A. Wood, Formation of chondritic refractory inclusions: The astrophysical setting. *Geochim. Cosmochim. Acta* **68**, 4007–4021 (2004). doi:10.1016/j.gca.2004.04.003

2. E. Jacquet, S. Fromang, M. Gounelle, Radial transport of refractory inclusions and their preservation in the dead zone. *Astron. Astrophys.* **526**, L8 (2011). doi:10.1051/0004-6361/201016118

3. F.C. Pignatale, S. Charnoz, M. Chaussidon, E. Jacquet, Making the planetary material diversity during the early assembling of the Solar System. *Astrophys. J. Lett.* **867**, 23 (2018). doi:10.3847/2041-8213/aaeb22

4. L. Yang, F. J. Ciesla, The effects of disk building on the distributions of refractory materials in the solar nebula. *Met. Planet. Sci* **47**, 99–119 (2012). doi:10.1111/j.1945-5100.2011.01315.x

5. L. Kööp, A. M. Davis, D. Nakashima, C. Park, A. N. Krot, K. Nagashima, T. J. Tenner, P. R. Heck, N. T. Kita, A link between oxygen, calcium and titanium isotopes in ^{26}Al-poor hibonite-rich CAIs from Murchison and implications for the heterogeneity of dust reservoirs in the solar nebula. *Geochim. Cosmochim. Acta* **189**, 70–95 (2016). doi:10.1016/j.gca.2016.05.014

6. J. N. Connelly, M. Bizzarro, A. N. Krot, Å. Nordlund, D. Wielandt, M. A. Ivanova, The absolute chronology and thermal processing of solids in the solar protoplanetary disk. *Science* **338**, 651–655 (2012). doi:10.1126/science.1226919 Medline

7. N. Kawasaki, C. Park, N. Sakamoto, S. Y. Park, H. N. Kim, M. Kuroda, H. Yurimoto, Variations in initial ^{26}Al/^{27}Al ratios among fluffy Type A Ca–Al-rich inclusions from reduced CV chondrites. *Earth Planet. Sci. Lett.* **511**, 25–35 (2019). doi:10.1016/j.epsl.2019.01.026

8. G. J. MacPherson, N. T. Kita, T. Ushikubo, E. S. Bullock, A. M. Davis, Well-resolved variations in the formation ages for Ca,Al-rich inclusions in the early Solar System. *Earth Planet. Sci. Lett.* **331-332**, 43–54 (2012). doi:10.1016/j.epsl.2012.03.010

9. L. Cieza, D. L. Padgett, K. R. Stapelfeldt, J.-C. Augereau, P. Harvey, N. J. Evans II, B. Merin, D. Koerner, A. Sargent, E. F. van Dishoeck, L. Allen, G. Blake, T. Brooke, N. Chapman, T. Huard, S.-P. Lai, L. Mundy, P. C. Myers, W. Spiesman, Z. Wahhaj, The *Spitzer* c2d survey of weak-line T Tauri stars. II. New constraints on the timescale for planet building. *Astrophys. J.* **667**, 308–328 (2007). doi:10.1086/520698

10. F. J. Ciesla, The distributions and ages of refractory objects in the solar nebula. *Icarus* **208**, 455–467 (2010). doi:10.1016/j.icarus.2010.02.010

11. N. Dauphas, M. Chaussidon, A perspective from extinct radionuclides on a young stellar object: The Sun and its accretion disk. *Annu. Rev. Earth Planet. Sci.* **39**, 351–386 (2011). doi:10.1146/annurev-earth-040610-133428

12. G. A. Brennecka, L. E. Borg, M. Wadhwa, Evidence for supernova injection into the solar nebula and the decoupling of *r*-process nucleosynthesis. *Proc. Natl. Acad. Sci. U.S.A.* **110**, 17241–17246 (2013). doi:10.1073/pnas.1307759110 Medline

13. N. Dauphas, E. A. Schauble, Mass fractionation laws, mass-independent effects, and isotopic anomalies. *Annu. Rev. Earth Planet. Sci.* **44**, 709–783 (2016). doi:10.1146/annurev-earth-060115-012157

14. K. D. McKeegan, A. P. A. Kallio, V. S. Heber, G. Jarzebinski, P. H. Mao, C. D. Coath, T. Kunihiro, R. C. Wiens, J. E. Nordholt, R. W. Moses Jr., D. B. Reisenfeld, A. J. G. Jurewicz, D. S. Burnett, The oxygen isotopic composition of the Sun inferred from captured solar wind. *Science* **332**, 1528–1532 (2011). doi:10.1126/science.1204636 Medline

15. T. S. Kruijer, C. Burkhardt, G. Budde, T. Kleine, Age of Jupiter inferred from the distinct genetics and formation times of meteorites. *Proc. Natl. Acad. Sci. U.S.A.* **114**, 6712–6716 (2017). doi:10.1073/pnas.1704461114 Medline

16. G. Budde, C. Burkhardt, G. A. Brennecka, M. Fischer-Gödde, T. S. Kruijer, T. Kleine, Molybdenum isotopic evidence for the origin of chondrules and a distinct genetic heritage of carbonaceous and non-carbonaceous meteorites. *Earth Planet. Sci. Lett.* **454**, 293–303 (2016). doi:10.1016/j.epsl.2016.09.020

17. P. H. Warren, Stable-isotopic anomalies and the accretionary assemblage of the Earth and Mars: A subordinate role for carbonaceous chondrites. *Earth Planet. Sci. Lett.* **311**, 93–100 (2011). doi:10.1016/j.epsl.2011.08.047

18. C. Burkhardt, T. Kleine, F. Oberli, A. Pack, B. Bourdon, R. Wieler, Molybdenum isotope anomalies in meteorites: Constraints on solar nebula evolution and origin of the Earth. *Earth Planet. Sci. Lett.* **312**, 390–400 (2011). doi:10.1016/j.epsl.2011.10.010

19. G. M. Poole, M. Rehkämper, B. J. Coles, T. Goldberg, C. L. Smith, Nucleosynthetic molybdenum isotope anomalies in iron meteorites—new evidence for thermal processing of solar nebula material. *Earth Planet. Sci. Lett.* **473**, 215–226 (2017). doi:10.1016/j.epsl.2017.05.001

20. Materials and methods are available as supplementary materials.

21. G. Budde, C. Burkhardt, T. Kleine, Molybdenum isotopic evidence for the late accretion of outer solar system material to Earth. *Nat. Astron.* **3**, 736–741 (2019). doi:10.1038/s41550-019-0779-y

22. J. A. M. Nanne, F. Nimmo, J. N. Cuzzi, T. Kleine, Origin of the non-carbonaceous–carbonaceous meteorite dichotomy. *Earth Planet. Sci. Lett.* **511**, 44–54 (2019). doi:10.1016/j.epsl.2019.01.027

23. C. Burkhardt, N. Dauphas, U. Hans, B. Bourdon, T. Kleine, Elemental and isotopic variability in Solar System materials by mixing and processing of primordial disk reservoirs. *Geochim. Cosmochim. Acta* **261**, 145–170 (2019). doi:10.1016/j.gca.2019.07.003

24. E. Jacquet, F. C. Pignatale, M. Chaussidon, S. Charnoz, Fingerprints of the protosolar cloud collapse in the Solar System. II. Nucleosynthetic anomalies in meteorites. *Astrophys. J.* **884**, 32 (2019). doi:10.3847/1538-4357/ab38c1

25. Q. R. Shollenberger, L. E. Borg, J. Render, S. Ebert, A. Bischoff, S. S. Russell, G. A. Brennecka, Isotopic coherence of refractory inclusions from CV and CK meteorites: Evidence from multiple isotope systems. *Geochim. Cosmochim. Acta* **228**, 62–80 (2018). doi:10.1016/j.gca.2018.02.006

26. A. M. Davis, L. Grossman, Condensation and fractionation of rare earths in the solar nebula. *Geochim. Cosmochim. Acta* **43**, 1611–1632 (1979). doi:10.1016/0016-7037(79)90181-9

27. P. J. Sylvester, B. J. Ward, L. Grossman, I. D. Hutcheon, Chemical compositions of siderophile element-rich opaque assemblages in an Allende inclusion. *Geochim. Cosmochim. Acta* **54**, 3491–3508 (1990). doi:10.1016/0016-7037(90)90300-A

28. G. Budde, T. Kleine, T. S. Kruijer, C. Burkhardt, K. Metzler, Tungsten isotopic constraints on the age and origin of chondrules. *Proc. Natl. Acad. Sci. U.S.A.* **113**, 2886–2891 (2016). doi:10.1073/pnas.1524980113 Medline

29. A. M. Davis, J. Zhang, N. D. Greber, J. Hu, F. L. H. Tissot, N. Dauphas, Titanium isotopes and rare earth patterns in CAIs: Evidence for thermal processing and gas-dust decoupling in the protoplanetary disk. *Geochim. Cosmochim. Acta* **221**, 275–295 (2018). doi:10.1016/j.gca.2017.07.032

30. L. Kööp, P. R. Heck, H. Busemann, A. M. Davis, J. Greer, C. Maden, M. M. M. Meier, R. Wieler, High early solar activity inferred from helium and neon excesses in the oldest meteorite inclusions. *Nat. Astron.* **2**, 709–713 (2018). doi:10.1038/s41550-018-0527-8

31. A. Trinquier, T. Elliott, D. Ulfbeck, C. Coath, A. N. Krot, M. Bizzarro, Origin of nucleosynthetic isotope heterogeneity in the solar protoplanetary disk. *Science* **324**, 374–376 (2009). doi:10.1126/science.1168221 Medline

32. J. Zhang, N. Dauphas, A. M. Davis, I. Leya, A. Fedkin, The proto-Earth as a significant source of lunar material. *Nat. Geosci.* **5**, 251–255 (2012). doi:10.1038/ngeo1429

33. T. S. Kruijer, T. Kleine, M. Fischer-Gödde, C. Burkhardt, R. Wieler, Nucleosynthetic W isotope anomalies and the Hf–W chronometry of Ca–Al-rich inclusions. *Earth Planet. Sci. Lett.* **403**, 317–327 (2014). doi:10.1016/j.epsl.2014.07.003

34. G. A. Brennecka, S. Weyer, M. Wadhwa, P. E. Janney, J. Zipfel, A. D. Anbar, $^{238}U/^{235}U$ variations in meteorites: Extant ^{247}Cm and implications for Pb-Pb dating. *Science* **327**, 449–451 (2010). doi:10.1126/science.1180871 Medline

35. G. Budde, T. Kruijer, T. Kleine, Hf-W chronology of CR chondrites: Implications for the timescales of chondrule formation and the distribution of ^{26}Al in the solar nebula. *Geochim. Cosmochim. Acta* **222**, 284–304 (2018). doi:10.1016/j.gca.2017.10.014

36. T. Kleine, C. Münker, K. Mezger, H. Palme, Rapid accretion and early core formation on asteroids and the terrestrial planets from Hf-W chronometry. *Nature* **418**, 952–955 (2002). doi:10.1038/nature00982 Medline

37. T. Kleine, K. Mezger, C. Münker, H. Palme, A. Bischoff, ^{182}Hf-^{182}W isotope systematics of chondrites, eucrites, and martian meteorites: Chronology of core formation and early mantle differentiation in Vesta and Mars. *Geochim. Cosmochim. Acta* **68**, 2935–2946 (2004). doi:10.1016/j.gca.2004.01.009

38. T. S. Kruijer, P. Sprung, T. Kleine, I. Leya, C. Burkhardt, R. Wieler, Hf–W chronometry of core formation in planetesimals inferred from weakly irradiated iron meteorites. *Geochim. Cosmochim. Acta* **99**, 287–304 (2012). doi:10.1016/j.gca.2012.09.015

39. N. Shirai, M. Humayun, Mass independent bias in W isotopes in MC-ICP-MS instruments. *J. Anal. At. Spectrom.* **26**, 1414–1420 (2011). doi:10.1039/c0ja00206b

40. M. Willbold, T. Elliott, S. Moorbath, The tungsten isotopic composition of the Earth's mantle before the terminal bombardment. *Nature* **477**, 195–198 (2011). doi:10.1038/nature10399 Medline

41. D. L. Cook, M. Schönbächler, High-precision measurement of W isotopes in Fe–Ni alloy and the effects from the nuclear field shift. *J. Anal. At. Spectrom.* **31**, 1400–1405 (2016). doi:10.1039/C6JA00015K

42. Qi-Lu, A. Masuda, The isotopic composition and atomic weight of molybdenum. *Int. J. Mass Spectrom. Ion Process.* **130**, 65–72 (1994). doi:10.1016/0168-1176(93)03900-7

43. M. Fischer-Gödde, T. Kleine, Ruthenium isotopic evidence for an inner Solar System origin of the late veneer. *Nature* **541**, 525–527 (2017). doi:10.1038/nature21045 Medline

44. R. C. J. Steele, C. D. Coath, M. Regelous, S. Russell, T. Elliot, Neutron-poor nickel isotope anomalies in meteorites. *Astrophys. J.* **758**, 59–80 (2012). doi:10.1088/0004-637X/758/1/59

45. C. Burkhardt, L. E. Borg, G. A. Brennecka, Q. R. Shollenberger, N. Dauphas, T. Kleine, A nucleosynthetic origin for the Earth's anomalous ^{142}Nd composition. *Nature* **537**, 394–398 (2016). doi:10.1038/nature18956 Medline

46. G. K. Nicolussi, M. J. Pellin, R. S. Lewis, A. M. Davis, R. N. Clayton, S. Amari, Zirconium and molybdenum in individual circumstellar graphite grains: New isotopic data on the nucleosynthesis of heavy elements. *Astrophys. J.* **504**, 492–499 (1998). doi:10.1086/306072

47. S. Gerber, C. Burkhardt, G. Budde, K. Metzler, T. Kleine, Mixing and transport of dust in the early solar nebula as inferred from titanium isotope variations among chondrules. *Astrophys. J.* **841**, L17–L24 (2017). doi:10.3847/2041-8213/aa72a2

48. J. Render, S. Ebert, C. Burkhardt, T. Kleine, G. A. Brennecka, Titanium isotopic evidence for a shared genetic heritage of refractory inclusions from different carbonaceous chondrites. *Geochim. Cosmochim. Acta* **254**, 40–53 (2019). doi:10.1016/j.gca.2019.03.011

49. G. A. Brennecka, T. Kleine, A low abundance of ^{135}Cs in the early Solar System from barium isotopic signatures of volatile-depleted meteorites. *Astrophys. J.* **837**, L9–L15 (2017). doi:10.3847/2041-8213/aa61a2

50. F. Moynier, J. M. D. Day, W. Okui, T. Yokoyama, A. Bouvier, R. J. Walker, F. A. Podosek, Planetary-scale strontium isotope heterogeneity and the age of volatile depletion of early solar system materials. *Astrophys. J.* **758**, 45 (2012). doi:10.1088/0004-637X/758/1/45

51. U. Hans, T. Kleine, B. Bourdon, Rb-Sr chronology of volatile depletion in differentiated protoplanets: BA-BI, ADOR and ALL revisited. *Earth Planet. Sci. Lett.* **374**, 204–214 (2013). doi:10.1016/j.epsl.2013.05.029

52. K. R. Bermingham, K. Mezger, S. Desch, E. E. Scherer, M. Horstmann, Evidence for extinct ^{135}Cs from Ba isotopes in Allende CAIs? *Geochim. Cosmochim. Acta* **133**, 463–478 (2014). doi:10.1016/j.gca.2013.12.016

53. J. A. Barrat, A. Jambon, M. Bohn, J. Blichert-Toft, V. Sautter, C. Göpel, P. Gillet, O. Boudouma, F. Keller, Petrology and geochemistry of the unbrecciated achondrite Northwest

Africa 1240 (NWA 1240): An HED parent body impact melt. *Geochim. Cosmochim. Acta* **67**, 3959–3970 (2003). doi:10.1016/S0016-7037(03)00092-9

54. G. J. MacPherson, "Calcium–aluminum-rich inclusions in chondritic meteorites" in *Meteorites and Cosmochemical Processes*, A. M. Davis, Ed., vol. 1 of *Treatise on Geochemistry*, H. D. Holland, K. K. Turekian, Eds. (Elsevier, ed.2, 2014), pp. 139–179.

55. G. A. Brennecka, M. Wadhwa, Uranium isotope compositions of the basaltic angrite meteorites and the chronological implications for the early Solar System. *Proc. Natl. Acad. Sci. U.S.A.* **109**, 9299–9303 (2012). doi:10.1073/pnas.1114043109 Medline

56. T. Kleine, U. Hans, A. J. Irving, B. Bourdon, Chronology of the angrite parent body and implications for core formation in protoplanets. *Geochim. Cosmochim. Acta* **84**, 186–203 (2012). doi:10.1016/j.gca.2012.01.032

57. Y. Amelin, A. Kaltenbach, T. Iizuka, C. H. Stirling, T. R. Ireland, M. Petaev, S. B. Jacobsen, U–Pb chronology of the Solar System's oldest solids with variable $^{238}U/^{235}U$. *Earth Planet. Sci. Lett.* **300**, 343–350 (2010). doi:10.1016/j.epsl.2010.10.015

58. E. A. Worsham, C. Burkhardt, G. Budde, M. Fischer-Gödde, T. S. Kruijer, T. Kleine, Distinct evolution of the carbonaceous and non-carbonaceous reservoirs: Insights from Ru, Mo, and W isotopes. *Earth Planet. Sci. Lett.* **521**, 103–112 (2019). doi:10.1016/j.epsl.2019.06.001

59. T. Yokoyama, C. M. O. D. Alexander, R. J. Walker, Assessment of nebular versus parent body processes on presolar components present in chondrites: Evidence from osmium isotopes. *Earth Planet. Sci. Lett.* **305**, 115–123 (2011). doi:10.1016/j.epsl.2011.02.046

60. Q. R. Shollenberger, A. Wittke, J. Render, P. Mane, S. Schuth, S. Weyer, N. Gussone, M. Wadhwa, G. A. Brennecka, Combined mass-dependent and nucleosynthetic isotope variations in refractory inclusions and their mineral separates to determine their original Fe isotope compositions. *Geochim. Cosmochim. Acta* **263**, 215–234 (2019). doi:10.1016/j.gca.2019.07.021

61. J. Render, G. A. Brennecka, S.-J. Wang, L. E. Wasylenki, T. Kleine, A distinct nucleosynthetic heritage for early Solar System solids recorded by Ni isotope signatures. *Astrophys. J.* **862**, 26 (2018). doi:10.3847/1538-4357/aacb7e

62. J. Render, M. Fischer-Gödde, C. Burkhardt, T. Kleine, The cosmic molybdenum-neodymium isotope correlation and the building material of the Earth. *Geochem. Persp. Lett.* **3**, 170–178 (2017). doi:10.7185/geochemlet.1720

63. Z. A. Torrano, G. A. Brennecka, C. D. Williams, S. J. Romaniello, V. K. Rai, R. R. Hines, M. Wadhwa, Titanium isotope signatures of calcium-aluminum-rich inclusions from CV and CK chondrites: Implications for early Solar System reservoirs and mixing. *Geochim. Cosmochim. Acta* **263**, 13–30 (2019). doi:10.1016/j.gca.2019.07.051